Science and Applications of Single-Nanotube Raman Spectroscopy

M. S. Dresselhaus,[a,][*] G. Dresselhaus,[b] A. Jorio,[c] A. G. Souza Filho,[d] Ge. G. Samsonidze,[e] and R. Saito[f]

[a] *Department of Electrical Engineering and Computer Science and Department of Physics, Massachusetts Institute of Technology, Cambridge, Massachusetts, 02139-4307, USA*

[b] *Francis Bitter Magnet Laboratory, Massachusetts Institute of Technology, Cambridge, Massachusetts, 02139-4307, USA*

[c] *Departamento de Física, Universidade Federal de Minas Gerais, Belo Horizonte, MG, 30123-970 Brazil, and Department of Physics, Massachusetts Institute of Technology, Cambridge, Massachusetts, USA*

[d] *Departamento de Física, Universidade Federal do Ceará, Fortaleza - CE, 60455-760 Brazil, and Department of Physics, Massachusetts Institute of Technology, Cambridge, Massachusetts, USA*

[e] *Department of Electrical Engineering and Computer Science, Massachusetts Institute of Technology, Cambridge, Massachusetts, 02139-4307, USA*

[f] *Department of Physics, Tohoku University, and CREST JST, Sendai 980-8578, Japan*

REVIEW

A review is presented of the resonance Raman spectra from individual isolated single-wall carbon nanotubes (SWNTs). A brief summary is given of how the measurements are made. Why the resonance Raman effect allows single-carbon nanotube spectra to be observed easily and under normal operating conditions is summarized. The important structural information that is provided by single-nanotube spectroscopy using one laser line is discussed, and what else can be learned from tunable laser experiments is reviewed. Particular attention is given to the determination of the nanotube diameter and of the energy of its van Hove singularities E_{ii}. Applications of single-nanotube spectroscopy are emphasized, such as measurements of isolated SWNTs connected with circuit-based samples and of isolated SWNTs mounted on an atomic force microscope tip. A critical assessment of the opportunities and limitations of the resonance Raman method for structural ($n1m$) identification is presented. The trigonal warping effect, which is central to the ($n1m$) identification in resonance Raman spectroscopy, is discussed in simple terms, and the importance of this effect in nanotube science and applications is reviewed.

Keywords: Single-Wall Carbon Nanotubes, Raman Spectroscopy, Single-Nanotube.

CONTENTS

1. INTRODUCTION

Because of the coupling between electrons and phonons under resonant conditions, phonons or lattice vibrations provide a sensitive probe of the remarkable electronic structure of single-wall carbon nanotubes (SWNTs), which can be either semiconducting or metallic, depending on their diameter and chirality.[1,2] Because of this strong electron-phonon coupling, resonance Raman spectroscopy is a selective characterization probe and is sensitive only to those nanotubes that are in resonance with the incident or scattered photon in the Raman process.

Because of this selective resonance effect, Raman spectroscopy has played an important role in characterizing the diameter distribution of SWNT bundles and has provided a probe that can distinguish between metallic and semiconducting nanotubes within a nanotube bundle.[3] Although resonance Raman spectroscopy has provided an important characterization tool for the diameter distribution of SWNT bundles, the main focus of this article, however, is in measuring the Raman spectrum from one individual nanotube. Single-nanotube spectroscopy opens up new possibilities for scientific spectroscopic studies and for the use of Raman spectroscopy as a structural characterization tool for individual SWNTs, so that other nanotube properties can be investigated at the single-nanotube level. Furthermore, understanding


M. S. Dresselhaus was born on November 11, 1930 in Brooklyn, NY and received her Ph.D. degree in physics from the University of Chicago in 1958. After a two-year postdoc at Cornell University, she came to MIT Lincoln Laboratory as a staff member and has been on the MIT faculty since 1967. She is an institute professor of electrical engineering and physics at MIT with broad interests in carbon science since 1961 and has been involved in carbon nanotube research since 1991 and carbon fiber research since 1980.
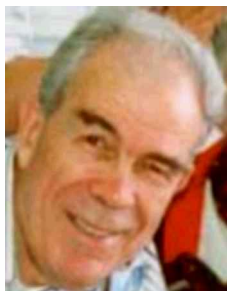
G. Dresselhaus was born on November 7, 1929 in Ancon, Panama Canal Zone, and received his Ph.D. degree in physics from the University of California in 1955. He served one year as an instructor at the University of Chicago and four years as an assistant professor at Cornell before joining MIT Lincoln Laboratory in 1960 as a staff member. In 1977 he transferred to the MIT Francis Bitter Magnet Laboratory, where he is currently a senior scientist. His area of interest is the electronic structure of solids. He also has been broadly involved in carbon research since 1955 and carbon nanotube research since 1991 and has co-authored with M. S. Dresselhaus several books on carbon materials.

A. Jorio was born on June 11, 1972, in Brazil and received his Ph.D. degree in physics from the Federal University of Minas Gerais, Brazil, in 1999. While completing his Ph.D., he spent one year (1998) working with Dr. Roland Currat at the Laue-Langevin Institute, France. He worked for two years (2000 and 2001) with Professor M. S. Dresselhaus at MIT as a postdoctoral fellow. He is currently an associate professor of physics at the Federal University of Minas Gerais, Brazil.
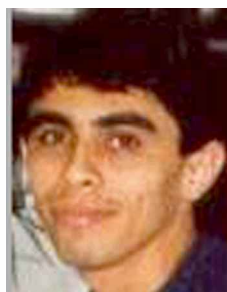
A. G. Souza Filho was born on June 12, 1975, in Brazil and received his Ph.D. degree in physics from the Federal University of Ceará, Brazil, in 2001. In 2001, he joined the Dresselhaus group at MIT as a Ph.D. visiting student, where he worked for 10 months on single-carbon-nanotube Raman spectroscopy. He is currently an associate researcher at the Federal University of Ceará, working on aspects of Raman scattering in solids.
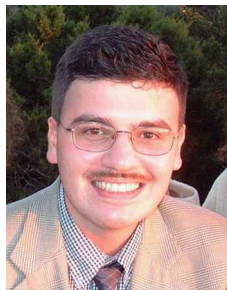
Ge. G. Samsonidze was born on August 8, 1976, in Russia and received his master's degree in physics from the St. Petersburg State Technical University, Russia, in 1999. He joined the Dresselhaus group in 2001 as a Ph.D. student in the Department of Electrical Engineering and Computer Science at MIT. He is currently working on single-carbon-nanotube Raman spectroscopy.

R. Saito was born on March 13, 1958, in Tokyo. He graduated (B.S.) from the University of Tokyo and earned his Ph.D. degree there in 1985. After being a research associate at the University of Tokyo, Saito was an associate professor at the University of Electro-Communication in Tokyo from 1990 to 2003 and recently was named full professor at Tohoku University in Sendai. He has worked extensively on the theory of carbon nanotubes since 1991 and has written a book on the subject, in collaboration with G. and M. S. Dresselhaus, *Physical Properties of Carbon Nanotubes*, published by Imperial College Press, in 1998. He was the recipient of the Japan IBM prize in 1999.

single-nanotube behavior gives new, detailed insights into the behavior of SWNT bundles, which have been proposed for use in various practical applications.

As explained in Section 2, the observation of resonance Raman spectra in carbon nanotubes (see Fig. 1)[4] arises from the very large density of electronic states that occurs in this one-dimensional nanostructured system at certain well-specified energies (see Fig. 2a). What is special about single-nanotube spectroscopy is that the unique connection between the geometrical structure of a nanotube and its electronic structure allows us to determine the geometrical structure of a nanotube at the single-nanotube level through the resonance Raman effect, as discussed in Section 2.

The main features of the Raman spectra (see Fig. 1a) are the *radial breathing mode*, where all of the atoms are moving in phase in the radial direction, and the *G-band modes*, which stem from the fundamental Raman-active mode in graphite. In addition, strongly dispersive modes, denoted by the *D-band* and its *harmonic G′-band*, are observed in carbon nanotubes, and these features are also observed in graphite and sp^2 carbons, along with lower intensity features, some of which are strongly dispersive and others that are weakly dispersive or nondispersive.

The structural determination provided by the resonance Raman effect allows us to study the dependence of each Raman feature on the nanotube diameter and chiral angle, as well as to obtain information about the intensity, linewidth, and polarization properties of each Raman feature; its dependence on laser excitation energy; and finally the connection between Raman spectra at the single-nanotube level and the corresponding Raman spectra normally observed for single-wall carbon nanotube bundles.

Section 2 presents the basic concepts behind the use of single-nanotube spectroscopy for structural characterization of a single nanotube, and in Section 3, experimental details are presented for carrying out Raman spectra on individual nanotubes. Details of the structural characterization determination are given in Section 4. Some examples of the use of single-nanotube spectroscopy in conjunction with other experiments are given in Section 5, and finally some of the unique properties of the Raman spectra of isolated carbon nanotubes are presented in Section 6, together with the relation between spectra for isolated SWNTs and those for SWNT bundles.

2. BASIC PHYSICAL CONCEPTS

A SWNT can be considered to be a single atomic layer of 2D graphite (called a graphene sheet) rolled up into a seamless cylinder. The structure of each nanotube is uniquely described by two integers (n, m), which refer to the number of $\vec{a}_1$ and $\vec{a}_2$ unit vectors of the 2D graphene lattice that are contained in the chiral vector, $\vec{C}_h = n\vec{a}_1 + m\vec{a}_2$, which spans the circumference of each nanotube.[2]
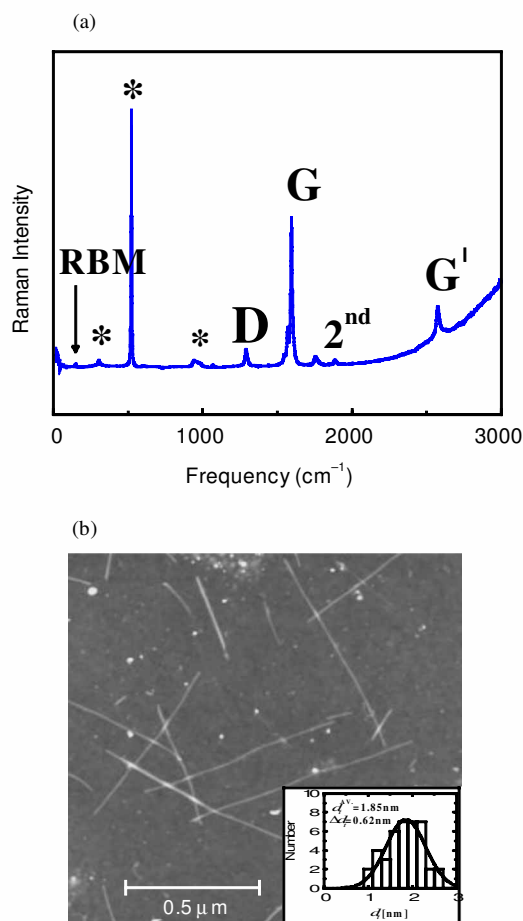

Fig. 1. (a) Raman spectrum from one nanotube taken over a broad frequency range, using $E_{laser} = 785$ nm $= 1.58$ eV excitation, showing the radial breathing mode (RBM), the *D*-band, the *G*-band, and the *G′*-band. Second-order modes are also observed but are not discussed in this review. The features marked with * at 303 cm⁻¹, 521 cm⁻¹, and 963 cm⁻¹ are from the Si/SiO₂ substrate[5] and are used for calibration of the nanotube Raman spectrum. The Si line at 303 cm⁻¹ can be identified as the second-order 2TA mode. (b) Atomic force microscope (AFM) image of the sample, showing isolated single-wall nanotubes grown from the vapor phase.[6] The small particles are iron catalyst particles. The inset shows the diameter distribution of this sample ($d_t = 1.85 \pm 0.62$ nm) based on AFM observations of 40 SWNTs.[4] Reprinted with permission from Ref. 4, A. Jorio et al., *Phys. Rev. Lett.* 86, 1118 (2001). © 2001, American Physical Society.

The chiral vector $\vec{C}_h$ together with the translation vector $\vec{T}$ along the nanotube axis and normal to $\vec{C}_h$ define the unit cell of the nanotube. Furthermore, from the (n, m) indices, one can directly determine the nanotube diameter d_t and the chiral angle θ. Using a convenient calculational method (to be discussed below), we can then calculate for each (n, m) nanotube the electronic energy bands, the density of electronic states,[2, 7] as well as the energies of the so-called van Hove singularities in the density of states, where the density of states is very high (see Fig. 2a). Because of the so-called trigonal warping effect of the constant energy contours of 2D graphite shown in Figure 2b, there is a weak dependence of the electronic
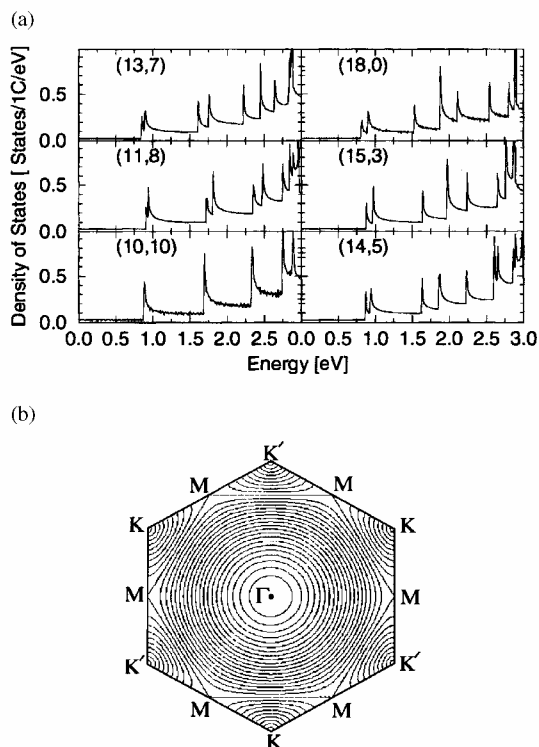
(a)

(b)

Fig. 2. (a) The 1D electronic density of states vs. energy (measured from the Fermi level) for several metallic nanotubes of approximately the same diameter, showing the effect of chirality and trigonal warping (see text) on the van Hove singularities in the density of states: (10, 10) (armchair), (11, 8), (13, 7), (14, 5), (15, 3), and (18, 0) (zigzag). Only the DOS for the conduction π^* band are shown; the mirror image of these plots gives the electronic density of states for the valence π band.[8, 9] The calculations are based on a simplified tight binding approximation (see text), assuming the energy overlap integral is $\gamma_0 = 2.9$ eV and the wave function overlap integral vanishes, $s = 0$ (Ref. 2). (b) Plot of the 2D equi-energy contours of 2D graphite, showing trigonal warping effects in the contours, as we move away from the K-point in the K–Γ or K–M directions. The equi-energy contours are circles near the K-point and near the center of the Brillouin zone. But near the M points on the zone boundary, the contours are straight lines that connect the nearest M points.[8, 10] Reprinted with permission from Ref. 11, R. Saito et al., *Phys. Rev. B* 64, 085312 (2001). © 2001, American Physical Society.

energy levels of SWNTs on the chiral angle θ, as well as a much stronger dependence on the nanotube diameter d_t, which determines the number of carbon atoms in the circular cross section of the nanotube shell, and this shell is one atom in thickness.[2]

The weak dependence of the electronic energy bands of SWNTs on the nanotube chiral angle θ relates to the wave vector k along the nanotube axis and to the 3-fold symmetry of the electronic dispersion relations of 2D graphite about the K-point of the 2D graphene Brillouin zone (see Fig. 2b), where the graphene valence and conduction bands are degenerate, forming a zero band-gap semiconductor.[2] Very close to the K-point, the graphene electronic energy bands exhibit circular constant energy contours, but as we move away from the K-point, a trigonal warping effect becomes apparent,[8, 11] as shown in

Figure 2b. This trigonal warping effect is responsible for the unique spectrum of singularities in the density of states of the conduction and valence bands for each (n, m) SWNT (Fig. 2a), when the energy bands of the graphene lattice are zone folded to form the energy bands of the SWNTs.[2, 8] This chirality dependence stems from the dependence of the direction of the nanotube axis on the (n, m) indices, thus leading to one-dimensional lines cutting the constant energy contours differently, depending on the (n, m) indices. The existence of the band degeneracy at the K-point and the presence of trigonal warping effects in graphite are based on symmetry considerations. These properties of the graphite electronic structure are general and are not specific to the calculational method used, whether it is based, for example, on first-principles approaches or on fitting experimental data to symmetry-based parameterized dispersion relations, as have been successfully used for many years in describing the electronic structure for graphite.[12]

The chirality dependence of the van Hove singularities[8, 9] in the 1D electronic density of states (DOS) of the conduction band, where the energy is measured relative to the Fermi energy, is shown in Figure 2a for several *metallic* (n, m) nanotubes, all having about the same diameter d_t (from 1.31 nm to 1.43 nm), but having different chiral angles: $\theta = 0°$, 8.9°, 14.7°, 20.2°, 24.8°, and 30.0° for nanotubes (18, 0), (15, 3), (14, 5), (13, 7), (11, 8), and (10, 10), respectively. The plot shows that as the chiral angle is varied from the armchair nanotube (10, 10) ($\theta = 30°$) to the zigzag nanotube (18, 0) ($\theta = 0°$), a splitting due to the trigonal warping effect (see Fig. 2b) develops in all of the singularities in the DOS.[8, 9] This splitting increases with decreasing chiral angle: it is zero for $\theta = 30°$ and reaches a maximum for $\theta = 0°$. Since the peak energies in the DOS (see Fig. 2a) are unique for each (n, m) value, the interband transition energies E_{ii} between the ith singularities in the valence and conduction bands are also unique. Here the integer i denotes a particular singularity in the joint DOS (JDOS), and i increases as the magnitude of the energy E_{ii} increases relative to the Fermi level E_F. A plot of E_{ii}, where the singularities in the JDOS occur, is presented in Figure 3a as a function of nanotube diameter d_t (Ref. 13). The resonance Raman effect is observed ideally when the incident or scattered photon energy is equal to E_{ii}. Plots of E_{ii} versus d_t are used extensively in single-nanotube Raman characterization studies to make the (n, m) identifications of individual isolated SWNTs. In practice, many Raman spectra are taken under preresonance conditions, when the incident or scattered photons are several meV or more away from E_{ii}.

As can be seen in Figure 3a, the trigonal warping effect causes a spread of the interband energies E_{ii} between the singularities in the JDOS for nanotubes with the same diameter d_t. The existence of a spread in E_{ii} at constant d_t is a general effect arising from the symmetry

of nanotubes and is not connected with any specific calculational scheme, though the specific energies E_{ii} and the magnitude of the spread both depend on the calculational technique. From the above discussion, we conclude that each nanotube (n, m) has a unique set of interband energies E_{ii} denoting the energy differences between the ith van Hove singularities in the conduction and valence bands. And, conversely, if one interband energy E_{ii} and a nanotube diameter d_t are specified (Fig. 3a),
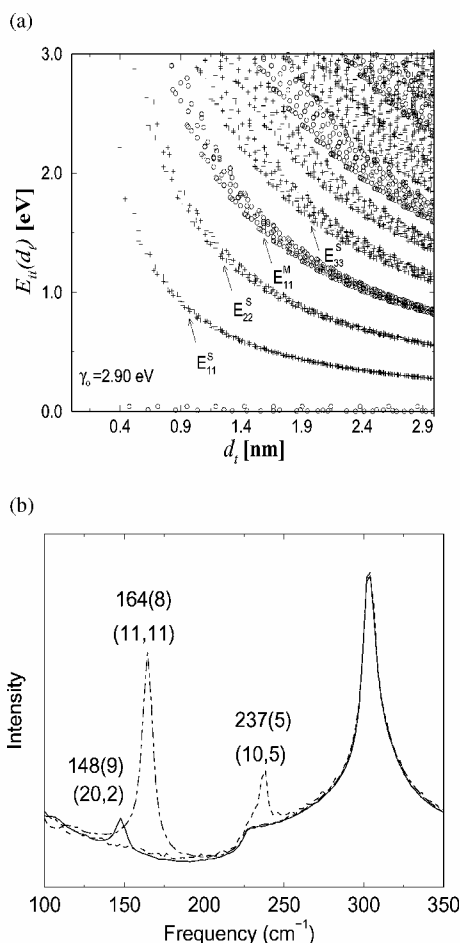

(a)

(b)

Fig. 3. (a) Calculated[13] energy separations E_{ii} between van Hove singularities i in the 1D electronic density of states of the conduction and valence bands for all (n, m) values versus nanotube diameter ($0.4 < d_t < 3.0$ nm), using a value for the carbon-carbon energy overlap integral of $\gamma_0 = 2.9$ eV and a nearest-neighbor carbon-carbon distance of $a_{C-C} = 1.42$ Å (Refs. 8 and 14). Semiconducting (S) and metallic (M) nanotubes are indicated by crosses and open circles, respectively. The index i in the interband transitions E_{ii} denotes the transition between the van Hove singularities, where $i = 1$ is closest to the Fermi level taken at $E = 0$. (b) The three Raman spectra (solid, dashed, and dash-dotted curves) come from three different spots on the Si substrate, showing the presence of only one resonant nanotube and one RBM frequency for each of the three laser spots. The RBM frequencies (widths) and the (n, m) assignments for each resonant SWNT are displayed. The 303 cm^{-1} feature comes from the Si substrate and is used for calibration of the SWNT spectra taken at $E_{laser} = 1.58$ eV (Ref. 4). Reprinted with permission from Ref. 4, A. Jorio et al., *Phys. Rev. Lett.* 86, 1118 (2001). © 2001, American Physical Society.

then its corresponding unique (n, m) can in general be identified, except for a possible energy degeneracy, which could occur when the energy E_{ii} value occurring for more than one tube is less than the experimental resolution (± 5 meV).

It is well established[2] that the (n, m) indices are crucial to the nanotube electronic structure. Most striking is the distinction between metallic and semiconducting nanotubes, namely the SWNTs for which $|n - m| = 3q$ are metallic, and those for which $|n - m| = 3q \pm 1$ are semiconducting, where q is an integer.[1,2] Thus we see that two-thirds of the bands in Figure 3a correspond to semiconducting nanotubes (S) and one-third to metallic nanotubes (M). Nevertheless, it has proved difficult to measure (n, m) experimentally and then to carry out property measurements on the same SWNT. We explain in Section 4 how the resonance Raman spectra from one isolated nanotube (as shown in Fig. 1a and Fig. 3b) can conveniently provide a determination of (n, m).

As stated above, a large enhancement in the Raman signal occurs in the resonance Raman effect, when the incident or scattered photon is in resonance or nearly in resonance with a singularity in the 1D JDOS of the SWNT, allowing the observation of a well-resolved Raman signal from an individual SWNT as shown in Figure 3b. This figure shows three Raman spectra in the low-frequency radial breathing mode region, taken for three different isolated SWNTs, each within a different light spot, about 1 μm in diameter, on a sample of isolated SWNTs, such as the one shown in Figure 1b. It is noteworthy that the intensity of the Raman signal from a strongly resonant tube, such as the (11,11) SWNT in Figure 3b, is comparable to that from the Si substrate, even though the SWNT signal comes from only a small fraction of the number of C atoms relative to the number of substrate Si atoms (C/Si $\sim 10^{-6}$) within the optical beam. This high sensitivity for SWNTs in resonance with the incident photon is the basis for the ability to observe a Raman spectrum from a single nanotube.

Having shown in Figure 3b that the resonance enhancement effect is sufficiently large to allow observation of the Raman spectrum from an individual isolated SWNT, we now summarize the necessary ingredients for carrying out an (n, m) determination from the measured Raman spectrum. From the experiment on isolated SWNTs on a Si/SiO$_2$ substrate, the radial breathing mode frequency, ω_{RBM}, is used to obtain the nanotube diameter according to the relation[2,3]

$$\omega_{RBM} = \alpha / d_t \qquad (1)$$

Theoretical determinations have been made of the proportionality constant α based on density functional theory ($\alpha = 234 \pm 2$ cm^{-1} nm),[15,16] whereas for SWNTs on the Si/SiO$_2$ substrate used in single-nanotube spectroscopy studies, α was experimentally found to be

REVIEW

248 ± 5 cm^{-1} nm by the measurement of ω_{RBM} on a large number (42) of isolated semiconducting and metallic SWNTs on a Si/SiO$_2$ substrate in the process of making a self-consistent evaluation of their (n, m) indices.[4] Furthermore, ω_{RBM} is not found to be dependent on the chiral angle θ to the accuracy of the measurements[17] and of the force constant calculations.[18]

In addition to determining d_t, it is necessary to have an experimental value for E_{ii} in order to determine (n, m) from Figure 3a. The evaluation of E_{ii} can be carried out in various ways and to various degrees of accuracy, but the important concern is to obtain sufficient accuracy to be able to distinguish the d_t and E_{ii} values of a given (n, m) tube from those of another (n', m') tube. The procedures that have been successfully used for the determination of E_{ii} are further discussed in Section 4. The assignment of the (n, m) values for d_t and E_{ii} also depends on theoretical calculations of E_{ii} and d_t for specific (n, m) SWNTs. For these calculations a symmetry-based model is used with fitting parameters for the electronic structure of 2D graphite that are adjusted to give a self-consistent interpretation of optical experiments, with particular emphasis given to the Raman spectrum from single nanotubes because of the high (5 meV) resolution of these experiments.

Because of the large anisotropy of the crystal structure, most models for the electronic structure of graphite start from a two-dimensional approximation, treating the intra-planar interaction between the $2s$, $2p_x$, $2p_y$ atomic orbitals to form strongly coupled bonding and antibonding trigonal orbitals. These trigonal orbitals give rise to three bonding and three antibonding σ-bands separated by ~ 10 eV in the two-dimensional graphite band structure. In these models, the weakly coupled p_z atomic wave functions correspond to two π-bands, which are degenerate by symmetry at the six Brillouin zone corners at points K and K' (see Fig. 2b), through which the Fermi level passes. A large number of calculations of the dispersion relations of the two-dimensional graphite electronic structure have been made with many calculational techniques and with various degrees of accuracy.[12] The various band models confirm the following features: (1) The 2D Fermi surface is located near the degenerate K and K' points of 3D graphite. (2) The widths of the π-bands in the vicinity of the K-point are much less than the separation between the π-bands and that between the bonding and antibonding σ-bands. Therefore two-dimensional band models involving only π-bands have been applied extensively to the qualitative interpretation of much experimental data relevant to the electronic structure of graphite near the Fermi level.

3. EXPERIMENTAL DETAILS

High-quality isolated SWNTs were grown on a slightly oxidized silicon substrate containing catalytic iron nanoparticles, with a chemical vapor deposition (CVD)

method. An example of the isolated SWNTs grown by the CVD method is shown in Figure 1b. The use of a slightly oxidized substrate is appropriate for low charge transfer between the nanotube and the substrate, and it is in fact such substrates that are used for transport measurements of SWNTs.[7] Although the interaction between the SWNTs and the substrate is expected to be weak, the van der Waals force between a nanotube and the substrate is sufficient to keep the nanotube in position so that it can be located on a Si substrate containing lithographic markers. The CVD process generates isolated SWNTs with diameters ranging from about 1 to 3 nm, according to atomic force microscopy (AFM) characterization (see inset to Fig. 1b). The density of SWNTs per μm^2 can be controlled during the growth process, basically through control of the time of growth. Sonication of SWNT bundle samples in solution can also form isolated SWNTs, but the sonication method is less appropriate for single-nanotube spectroscopy studies, since small bundles persist after sonication, and some introduction of nanotube defects and nanotube fracturing occurs through the sonication process itself.

Resonance Raman spectra from isolated SWNTs can be measured in the 100 cm^{-1} to $\sim$3000 cm^{-1} spectral range with standard commercial micro-Raman spectrometers and lasers including systems connected with central user facilities. In our work, we measured the Raman spectra from isolated SWNTs with a Renishaw (1000B) spectrometer, a Kaiser (Hololab 5000R) single-monochromator micro-Raman spectrometer, and a Dilor XY triple-monochromator micro-Raman spectrometer, using a back-scattering configuration for all measurements and 50×, 80×, and 100× objective lenses.

Relatively high laser powers can be used to probe isolated SWNTs because of their unusually high thermal conductivity,[19] their excellent high temperature stability, and their good thermal contact with the substrate. A triple monochromator is ideal for the Raman measurements while the excitation laser line is tuned continuously, but the acquired intensity drops substantially when compared with the intensity obtainable from a single-monochromator spectrometer. We have measured the Raman spectra from over 200 isolated SWNTs, using discrete lines from an Ar-Kr laser and a continuous range of excitation energies from both a Ti:sapphire and a dye laser. We have observed stable nanotube Raman signals for laser powers impinging on the substrate up to 40 mW into a 100× objective. We usually use laser powers of about 10–20 mW in our measurements, although measurements have been carried out successfully with laser power levels down to 1 mW.

In the process of measuring the Raman spectra from isolated SWNTs on a Si/SiO$_2$ substrate with a fixed laser energy E_{laser}, we focus the laser spot on the substrate surface, and we scan the sample until we observe the Raman signal from an isolated SWNT. The Raman intensity from

SWNTs is usually buried under the noise, except for a few (n, m) SWNTs for which the resonance with the given E_{laser} occurs strongly for the electronic states confined within the van Hove singularities. The observation of the weak Si feature at 303 cm^{-1} (see Fig. 1a) is a useful guide for knowing whether the radial breathing Raman mode from an isolated SWNT can be measured. Samples with a high nanotube density (more than 1 SWNT/μm^2) guarantee that the search for resonant nanotubes will not be so tedious, but a low-density sample (less than 1 SWNT/μm^2) guarantees that one will not get a Raman signal from two or more SWNTs within the same light spot. For various experiments of interest, we have used samples with a variety of nanotube densities, ranging from low-density samples ($\sim$0.4 SWNT/μm^2) to higher-density samples ($\sim$10 SWNT/μm^2).

Since the resonance Raman intensity from isolated SWNTs is a maximum for incident and scattered light polarized along the tube axis, it is helpful to optimize the signal by using a $\lambda/2$ wave plate to rotate the polarization of the incident and scattered light.[20] Attention to the polarization of the light is important for carrying out quantitative studies of the Raman intensity.

The Raman features are analyzed by a Lorentzian fit of the spectra, with the exception of the lower-frequency G-band feature for metallic SWNTs, denoted by G^-, which is observed to have a Breit–Wigner–Fano (BWF) lineshape. Though it is known that the D and G' bands appear in the Raman spectra of graphite-like materials through a double resonance process,[21, 22] where inhomogeneous broadening occurs, we use the Lorentzian fit as an approximation to estimate the behavior of the D and G' bands.

4. STRUCTURAL (n, m) CHARACTERIZATION OF SWNTs

From Section 2 we concluded that the determination of the structural (n, m) indices of a SWNT depends on the experimental measurement of the nanotube diameter d_t and the energy E_{ii} of the van Hove singularity in the JDOS, exploiting the unique relation between (n, m) and (d_t, E_{ii}) through the electronic structure of SWNTs on (n, m) (Ref. 2). As stated above, the determination of d_t follows from measurements of ω_{RBM} from the Raman spectra and the use of Eq. (1). The determination of E_{ii} can, in principle, be carried out simply by using a tunable laser to bring E_{laser} into perfect resonance with E_{ii}, where the maximum intensity in the Raman spectrum occurs at $E_{ii} = E_{laser}$. In practice, such a tunable laser system has thus far only been applied in one instance to single-nanotube Raman spectroscopy studies,[23] and even in this case the measurements were made over only a small energy range ($\sim$0.15 eV) with the use of a tunable Ti:sapphire laser.[23]

Even though a tunable laser may not be available for most user groups, it is still possible to find isolated SWNTs for which an (n, m) determination can be made, provided that the nanotube is within the resonant window of a single available laser excitation line, which in practice is satisfied for E_{laser} within $\sim \pm 0.1$ eV of an interband transition for that nanotube. From the measured ω_{RBM} and the use of Eq. (1), the nanotube diameter d_t is found, and the i index in E_{ii} can be found from Figure 3a. However, an accurate determination of the value of E_{ii} is more challenging.

One method for determining the magnitude of E_{ii} directly requires measurement of both radial breathing mode spectra for the Stokes and anti-Stokes processes.[24, 25] This procedure is very sensitive to E_{ii}, even when the ω_{RBM} values for two or more SWNTs are very close to each other. We illustrate such a case with the semiconducting tubes $(12, 1)$ and $(11, 3)$ shown in Figure 4a and b, respectively. Even though it is not possible to distinguish between the two tubes from their measured ω_{RBM} values, the ratio of the anti-Stokes to Stokes intensities I_{AS}/I_S for their radial breathing modes is very different, as seen in the experimental traces in Figure 4, and this large difference in I_{AS}/I_S at the energy E_{laser} is then used to sensitively (to 10 meV accuracy) determine the energy E_{ii} by a fitting process, as done in the lower panels of Figure 4, to get the calculated and measured I_{AS}/I_S ratios at the energy E_{laser} to agree. As shown in Figure 4, although the tubes $(12,1)$ and $(11,3)$ have very similar d_t values, they have very different experimental E_{22}^S values of 1.587 eV and 1.554 eV, respectively, as deduced from the procedure described.[24]

The E_{ii} determination for an isolated nanotube can be carried out even more simply by using a single-laser excitation energy E_{laser} when the nanotube is in approximate resonance with E_{laser}, by (1) measuring the intensity of the radial breathing mode, (2) calculating the E_{ii} values of various candidate (n, m) nanotubes with similar d_t values, as determined by the frequency of the radial breathing mode, and (3) then making a comparison between the relative RBM intensities of the test SWNT with the intensities of other SWNTs whose (n, m) indices have previously been determined (and consequently their experimentally determined d_t and E_{ii} values have also been matched to calculated values). When this very simple method is used for the (n, m) identification, we normally check the tentative (n, m) assignment by considering the characteristics of the other features in the Raman spectra, such as the G-band and the G'-band, that are sensitive to (n, m).[17] If the (n, m) values of every nanotube in the sample must be found, then a tunable laser is needed to provide a resonant excitation energy for each nanotube, so that a complete (n, m) Raman characterization can be carried out for each SWNT.

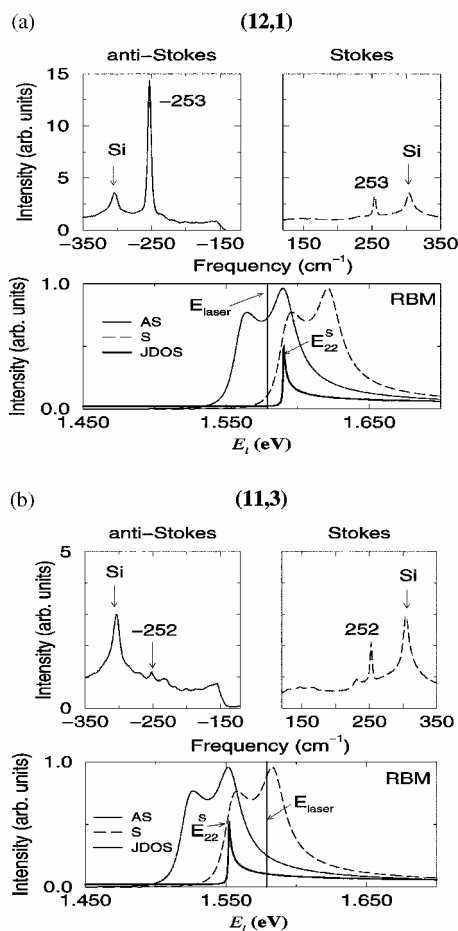In the one example where a tunable laser was used to measure E_{ii} by tuning E_{laser} through the resonance

REVIEW

Fig. 4. (a) Resonance anti-Stokes (AS) and Stokes (S) spectra for a (12,1) semiconducting SWNT on a Si/SiO$_2$ substrate, using 1.579 eV (785 nm) laser excitation (upper panels) and the predicted JDOS (heavy line) and resonant windows for the RBM mode in the anti-Stokes (solid line) and Stokes (dashed line) processes for the (12,1) SWNT (lower panel). (b) As in (a), except that the data are for the (11,3) SWNT. The energy E_{22}^S in (a) and (b) in the lower panels is varied to obtain the experimentally measured I_{AS}/I_S ratio given in the upper panels of (a) and (b), where the AS spectra are normalized by the Boltzmann factor for easy comparisons of the relative AS and S intensities. The laser excitation energy ($E_{laser} = 1.579$ eV) is indicated by the vertical solid lines in the two lower figures.

Fig. 5. Raman intensity versus laser excitation energy E_{laser} for $\omega_{RBM} = 173.6$ cm^{-1} peak in the Stokes (S) and anti-Stokes (AS) Raman processes of an isolated (18, 0) SWNT, where the AS intensity is normalized by $\exp(\hbar\omega_{RBM}/k_B T)$ to facilitate comparisons with the S profile. The solid circles and squares represent two different E_{laser} runs on the same SWNT sample. The line curves indicate the resonant Raman windows predicted from Eqs. (2) and (3), with $E_{ii} = 1.655$ eV, $\Gamma_r = 8$ meV, and $\Gamma_J = 0.5$ meV. The upper inset compares the theoretically predicted S and AS resonant windows. The lower inset plots the JDOS profile for the two lowest energy van Hove singularities for one isolated (18, 0) SWNT with $\Gamma_J = 0.5$ meV (Ref. 23). Reprinted with permission from Ref. 23, A. Jorio et al., *Phys. Rev. B* 63, 245416 (2001). © 2001, American Physical Society.

frequency (Fig. 5), not only was E_{ii} measured, but an experimental determination was also obtained for the spectral profile of the 1D JDOS for an individual SWNT near a van Hove singularity. This spectral profile gives direct evidence for the sharp singularities in the JDOS, showing how it is possible to get sufficient intensity to observe a Raman spectrum from just one nanotube.[23]

Many physical properties, such as transport, optical, and mechanical properties, are very sensitive to the spectral profile of the electronic DOS, but the profile is difficult to measure directly, because probes, such as scanning tunneling microscopy (STM) tips,[26] interact too strongly with the nanotube, thereby broadening the van Hove singularities (from less than 1 meV to more than 10 meV) and consequently broadening the DOS that is probed by
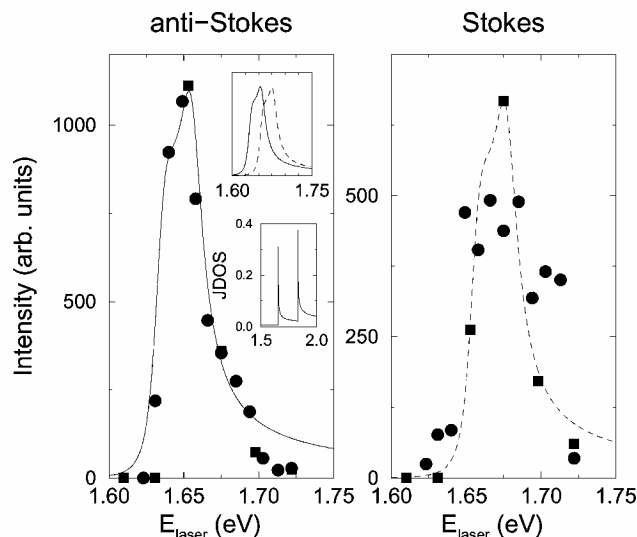
scanning probe methods.[26] It is for this reason that the measurement of the profile of the JDOS by a weakly interacting probe is so important.

The JDOS spectral profile and the (n, m) value of the SWNT were determined by measuring the resonant S and AS Raman spectrum for this nanotube for many different frequencies, thus obtaining a reliable determination of E_{ii} (to ± 3 meV) as well as of the parameters of the spectral profile (Fig. 5). The experiments were carried out on a sample containing lithographic markers, so that as E_{laser} was tuned, the microscope focus could always be brought to the same nanotube. The RBM integrated intensity $I(E_{laser})$ is a function of E_{laser} and can be evaluated from the JDOS $g(E)$ according to

$$I(E_{laser}) = \int \left| \frac{M}{(E_{laser} - E - i\Gamma_r)(E_{laser} \pm E_{ph} - E - i\Gamma_r)} \right|^2$$
$$\times g(E)dE \qquad (2)$$

in which the first and second factors in the denominator, respectively, describe the resonance effect with the incident and scattered light, where the $+$ ($-$) applies to the AS (S) process for a phonon of energy E_{ph}, whereas Γ_r gives the inverse homogeneous lifetime for the resonant scattering process and includes contributions from many processes, such as internal relaxation, possible vibronic

phonon structure in E_{ii}, temperature broadening effects, and coupling with the radiation field. The matrix element in Eq. (2) for the scattering process $M = M_i M_{ep} M_s$ is considered, for simplicity, to be independent of E. Here M_i, M_s, and M_{ep} are, respectively, matrix elements for the electron-radiation absorption, the electron-radiation emission, and the electron-phonon interaction, and the JDOS $g(E)$ can be approximated within the one-electron theory by the asymmetric profile

$$g(E) = \mathrm{Re}\left[\sum_i \frac{a_{C-C} E}{d_t \gamma_0 \sqrt{[(E - E_{ii} - i\Gamma_J)(E + E_{ii} + i\Gamma_J)]}} \right] \tag{3}$$

where $a_{C-C} = 0.142$ nm is the nearest-neighbor distance between carbon atoms, γ_0 is the tight binding energy overlap integral, and Γ_J is introduced as a measure of the effect on the width of the JDOS singularity for the E_{ii} electronic transition of the nanotube finite length and of the finite size of the laser beam on the nanotube, reflecting a finite number of effective wave vectors along the tube length. To some extent Γ_J depends on the characteristics of the individual SWNT but should have approximately the same value from one tube to another, assuming that the laser spot on the tube is less than its length. The i in front of Γ_j in Eqn. (3) is not a van Hove singularity index, but instead is a complex unit imaginary. The value of $\gamma_0 = 2.90 \pm 0.02$ eV provides a good fit to a large body of experimental optical and Raman data.[4, 27] The sum over i takes into account the different van Hove singularities of one SWNT (see Fig. 2a), being very important for metallic tubes when the trigonal-warping-induced splitting is small.

Experimentally, a fit of the data points in Figure 5 determines the values of the fitting parameters in Eqs. (2) and (3), showing that Γ_r (~ 8 meV) is most sensitive to determining the FWHM linewidth of the spectral features, but that the very small value of Γ_J (~ 0.5 meV) gives rise to the very strong intensity enhancement (~ 1000) associated with the sharp 1D van Hove singularities in the JDOS $g(E)$. Once the parameters in Eqs. (2) and (3) are found, the spectral profile of the JDOS can be plotted, as in the inset to Figure 5, where $g(E)$ is seen to be highly asymmetric and to have very sharp singularities. Measurements of the S and AS spectra over the whole resonance window (~ 100 meV) of the nanotube yield the E_{ii} value more accurately (to 5 meV) than when a single laser line is used (~ 10 meV accuracy). Further measurements of the profile of the electronic density of states are needed to determine whether the profile is the same for semiconducting and metallic tubes and to establish in more detail the functional form for $g(E)$.

The reliability of the (n, m) assignment using resonance Raman spectroscopy depends on the accuracy of the experimental determination of the nanotube diameter and of the E_{ii} value[24] as well as the use of a theoretical model to relate d_t and E_{ii} to (n, m).[9, 28, 29] We comment

on each of these issues separately. The determination of the nanotube diameter depends on knowing the proportionality constant α, in $\omega_{RBM} = \alpha/d_t$, accurately. For the isolated SWNT resonance Raman spectroscopy studies we have chosen to place the SWNTs on a slightly oxidized smooth silicon wafer substrate to minimize the interaction between the SWNT and the substrate, as discussed in Section 3. For these experimental conditions, the proportionality constant α was determined to have a reliability of 248 ± 5 cm^{-1} nm through a self-consistent fitting of the (n, m) indices initially for 42 SWNTs[4] and subsequently for over 100 other SWNTs.[30, 31] The second ingredient, the experimental determination of E_{ii}, is described above in Section 4.

The third ingredient in the fitting procedure is a theoretical model to relate (n, m) to E_{ii}. Since first-principles band structure calculations are often not accurate enough to model detailed experimental data that are available for graphite and SWNTs near the Fermi level, symmetry-based (Slater–Koster-type) models are most often used to fit experimental data quantitatively.[12] A similar approach has been taken to interpret the Raman spectra of SWNTs at the single-nanotube level. Up to now, the simplest version of the symmetry-based models has been used, namely taking the nearest-neighbor transfer integral t as a fitting parameter and setting the nearest-neighbor overlap integral $s = 0$ (Ref. 2). This approximation makes the valence and conduction bands for SWNTs symmetrical relative to the Fermi level, which is quite different from these for graphite.[2] It should be mentioned that the Slater–Koster approach uses normalized wave functions and in this sense differs somewhat from the tight banding model in general. Exciton effects and effects due to nanotube curvature have not yet been included in symmetry-based models.

For the (n, m) identification based on the radial breathing mode in the resonance Raman spectra, a symmetry-based Slater–Koster type model has been used with band parameters, based on rolling a 2D graphene sheet to form a nanotube, but modified to fit the resonance Raman experiments under consideration. The experimental determination of the nearest-neighbor transfer integral t (or of the energy overlap integral γ_0 of the Slater–Koster-type Slonczewski–Weiss–McClure model, in the commonly used notation for graphite[12]) is based on analysis of the Raman spectra themselves.[14, 17, 22] In this analysis, the distance between nearest carbon atoms $a_{C-C} = 0.142$ nm in SWNTs is based on transmission electron microscopic (TEM) measurements, leading to the values $|t| = \gamma_0 = 2.90$ eV for SWNTs (since $s = 0$ in the present approximation, we can write $\gamma_0 = |t|$), which should be compared with $\gamma_0 = 3.13$ eV for graphite.[12] This γ_0 value for SWNTs is found to describe a number of other optical experiments well, such as, for example, optical absorption studies on SWNT bundles,[32] the asymmetries in the S versus AS Raman measurements on SWNTs,[24, 33−35] the oscillatory behavior of the RBM spectral moments,[36]

the oscillation in the dispersive *D*-band frequencies for SWNT bundles,[37] and the unusual *G*-band[38] and *G'*-band[39] spectral features. In fact, all of the information provided by the *G*-band, *D*-band, and *G'*-band Raman features regarding nanotube diameter and chirality can be used to corroborate the (n, m) assignment proposed by the analysis of the RBM feature.[17] However, scanning tunneling microscopy/spectroscopy (STM, STS) experiments are better described with the $\gamma_0 \sim 2.6$ eV value,[7] and the origin for the different γ_0 values likely stems from both the different electron excitation states that are involved in the two experiments and the simplified form that has been used thus far for the Slater–Koster approximation to the electronic energy band structure for SWNTs.

Further experimental work is needed, such as joint STS/STM and TEM and Raman spectroscopy measurements on the same physical (n, m) nanotube, to improve our modeling capabilities. It is expected that the symmetry-based models can then be refined by introducing at least one more nonzero fitting parameter, by accounting for differences in the participating electronic states, and by taking account of curvature effects explicitly. In these symmetry-based models, the numbers of terms used in the Fourier expansion of the energy bands (or of the phonon dispersion relations) depends on the amount and accuracy of the available experimental data that are used in the fitting of the energy levels (or the phonon dispersion relations). Furthermore, the present models based on graphitic π-bands are expected to work better for SWNTs with diameters larger than ~ 1.0 nm and to become less valid as d_t decreases. When accurate first–principles calculations become available for specific (n, m) SWNTs, the results of these calculations can be used to further refine the parameters of the Slater–Koster symmetry-based models, which are applicable for SWNTs of any (n, m), whether or not first-principles calculations have been carried out for that particular (n, m). With the current synthesis techniques for carbon nanotubes, a very large distribution of diameters and chiral angles is contained within a particular SWNT bundle sample, and the Slater–Koster model is the only technique currently available for modeling this large number of different SWNTs.

5. JOINT STUDIES AT THE SINGLE-NANOTUBE LEVEL

In this section we discuss how the resonance micro-Raman characterization tools for the (n, m) identification of individual isolated SWNTs can be further used for the study of other properties of individual SWNTs on the single-nanotube level, either involving different experimental techniques or for the applications of SWNTs in nanodevices. One serious challenge in performing more than one experiment on the same SWNT is to localize the tube spatially so as to be able to return to the same nanotube many times and to provide a physical environment

and a spatial localization procedure for the nanotube that is compatible with both carrying out the properties measurement and the Raman characterization measurement.

One direct method for finding a specific nanotube and for then using resonance Raman spectroscopy for the characterization of that nanotube, and later returning to the same SWNT that will later be used for other studies, is to prepare a lithographically marked sample on the same Si/SiO$_2$ substrate, where a low density of SWNTs is deposited. The first measurement could be the structural (n, m) characterization by Raman spectroscopy, and subsequent measurements could then be made on the same nanotube, with the use of either Raman spectroscopy or another experimental technique. For example, one study that made use of a lithographically marked sample was the study of the radial breathing mode on the same nanotube with different laser lines.[23] Other examples of this approach might be Raman measurements of different Raman features on the same nanotube, perhaps at different E_{laser} lines, at different temperatures, and under other conditions.

The next example involves a simple technique for making fiduciary markers that allows easy return to the same physical nanotube. Figure 6 shows a simple experimental procedure for spatially localizing a particular SWNT with the use of markers made on the substrate with a diamond tip, as shown in the optical image (50×) of Figure 6a. AFM images can be taken on such a sample to describe the surface and to identify the presence of isolated SWNTs (see Fig. 6b). The density of isolated SWNTs deposited on the Si substrate can be controlled by the catalyst formation and by timing the SWNT growth procedure. A very low density of isolated SWNTs on the
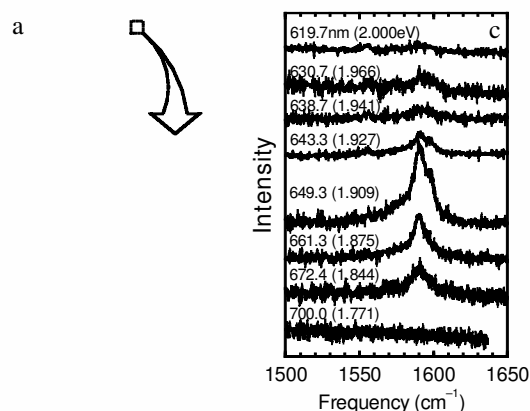

Fig. 6. (a) An optical image of a Si/SiO$_2$ substrate with markers made by a diamond scribe. (b) An AFM image of a nanotube, located near the edge of one marker, located near one isolated SWNT that is probed by resonant Raman spectroscopy. (c) *G*-band Raman spectra of the isolated SWNT shown in (b) for various laser excitation energies (and equivalent wavelengths) provided by a DCM dye laser.[40] Reprinted with permission from Ref. 40, A. Jorio et al., *Braz. J. Phys.* 32, 921, (2002). © 2002, American Physical Society.

surface of this sample (Fig. 6b) makes it easy to identify the tube that is resonant with E_{laser}. Raman spectra were taken at the position of the isolated SWNT shown in Figure 6b, close to the diamond marker. Figure 6c shows the *G*-band Raman spectra from this SWNT, obtained with different laser lines from a DCM dye laser. With the use of the diamond marker, it was possible to always return to the same SWNT and to find the E_{ii}.[40] Therefore, the use of a low-nanotube-density sample with diamond markers on the substrate makes it relatively easy to analyze the same isolated SWNT with different techniques, that is, AFM and Raman spectroscopy.

We now give an example of a situation for which the nanotube experiment requires its own sample holder, such as an AFM experiment. In this example, suppose that the goal of this experiment might be the characterization by TEM, AFM, and Raman spectroscopy of the same SWNT (which is to be used for an AFM tip). Figure 7a shows an optical image ($100\times$) obtained from a Si AFM tip containing a SWNT at the edge (upper left inset shows a TEM image of a Si-SWNT AFM tip, taken from Ref. 6). Figure 7b shows Raman spectra obtained by focusing the laser at the edge of an AFM tip on which a SWNT is mounted. From the RBM frequency ω_{RBM}, we can obtain the nanotube diameter ($d_t = 248/\omega_{RBM}$).[4] The interband electronic transition energy E_{ii} involved in the resonant Raman scattering process of the measured SWNT can also be obtained, since the Raman intensity is proportional to the JDOS.[23, 24] For the SWNT spectra shown in Figure 7b, resonance with this nanotube was found with an Ar:Kr laser, with laser excitation energies $E_{laser} = 2.18$, 2.41, and 2.54 eV. For this nanotube, the resonance occurs near $E_{laser} = 2.41$ eV, where $\omega_{RBM} = 196$ cm^{-1} is clearly measured ($d_t = 248/196 = 1.27$ nm), and the SWNT at the AFM tip was assigned as the $(16, 0)$ SWNT.[4]

6. UNIQUE ASPECTS OF SINGLE-NANOTUBE SPECTROSCOPY

Up to this point we have focused on the unique properties of the RBM of carbon nanotubes because of the importance of the RBM in the use of Raman spectroscopy for the structural characterization of carbon nanotubes. This phonon mode, which is associated with the coherent atomic breathing motions of all the carbon atoms in the nanotube in the radial direction, is also special to carbon nanotubes and is not observed in other carbon forms. In this section, we briefly consider all of the other dominant features in the Raman spectra.

Many of the unique properties of carbon nanotubes relative to graphite and other sp^2 carbons stem from the 1D aspects of the structure of nanotubes and from the nanotube curvature. In this section we review why the 1D aspects are so important for distinguishing carbon nanotubes from graphite and how this leads to many of the unique phenomena observed in the Raman spectra of SWNTs. In Sections 2 and 4, we reviewed the effect of low dimensionality in producing singularities in the electronic DOS, resulting in unique strong resonance effects for all features in the Raman spectra because of the strong coupling between electrons and phonons under these strong resonance conditions. In this section we emphasize the strong resonance effects for the most intense Raman features.

6.1. Symmetry Considerations

The 1D aspects of small-diameter nanotubes also give rise to a small number of quantized parallel wave vectors (cutting lines) making an angle $\phi = \pi/6 - \theta$ with the KK' direction in the Brillouin zone (see Fig. 8), so that $\phi = 0$ for armchair (n, n) tubes and $\phi = \pi/6$ for zigzag $(n, 0)$ tubes. For zigzag nanotubes, for example, the number of cutting lines is equal to the number of carbon atoms in the circumferential direction. Thus, as the diameter of the nanotubes increases, the number of cutting lines increases
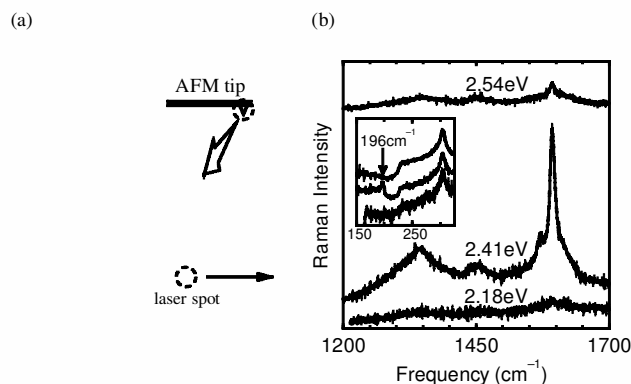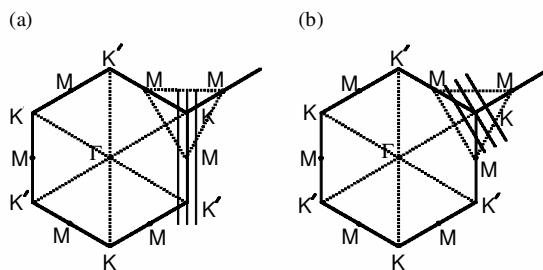

Fig. 7. (a) The optical image of a Si-SWNT AFM tip. One isolated SWNT is attached to the edge of the Si tip by the procedure discussed in Ref. 6. The upper left inset shows a TEM image of another Si-SWNT AFM tip, taken from Ref. 6. (b) SWNT *G*-band Raman spectra obtained with three laser lines focused at the edge of the Si tip shown in the optical image (a). The inset shows the corresponding RBM frequency region for the three laser lines used for the *G*-band spectra.[40] Reprinted with permission from Ref. 40, A. Jorio et al., *Braz. J. Phys.* 32, 921 (2002). © 2002, Brazil Physical Society.

Fig. 8. The dependence of the trigonal warping effect of the van Hove singularities on the nanotube chirality. The three bold lines near the *K* point denote three possible quantized *k* vectors in the hexagonal Brillouin zone of graphite for metallic (a) armchair and (b) zigzag carbon nanotubes. All chiral nanotubes with chiral angles $|\theta| \leq \pi/6$ have cutting lines for their quantized *k* vectors with directions making a chiral angle θ measured from the bold lines for the zigzag nanotubes.

proportionally, and their spacing decreases, giving rise to diameter-dependent effects on all Raman features sensitive to the resonance with the electronic states near a van Hove singularity. Along the tube axis, the wave vectors remain continuous, as in a graphene sheet. Because of the trigonal warping of the constant energy contours, the spacing between the intersections of these constant-energy contours with adjacent cutting lines will depend on chirality as well as on diameter, as discussed in Sections 2 and 4.

The resulting dependences of nanotube properties on nanotube diameter and chirality apply to all important features of the Raman spectra of carbon nanotubes. The diameter and chirality-dependent effects related to these symmetry considerations can only be studied quantitatively at the single-nanotube level under properly controlled conditions.[17, 31] What is seen for SWNT bundles is an average over the contributions from the (n, m) nanotubes contained in the SWNT bundle sample, yielding effects different from those for graphite, but also different from those for isolated SWNTs, as summarized subsequently (see Section 6.3). For example, individual isolated nanotubes exhibit sharp Lorentzian lineshapes, with (FWHM) linewidths down to $4 \, \text{cm}^{-1}$ (or down to $3 \, \text{cm}^{-1}$ after deconvolving the instrument function) for the radial breathing-mode, whereas SWNT bundles typically show a broad radial breathing-mode spectrum reflecting the superposition of the many nanotubes that are within the resonant window (~ 0.1 eV) for a given laser line.[42] Thus by making measurements over many laser lines (see Fig. 9) and modeling the (n, m) values for E_{ii} that could be expected for each E_{ii}, based on an E_{ii} versus d_t plot, as shown in Figure 3a, oscillations can be observed in the frequency where the maximum intensity of the radial breathing mode occurs for a given SWNT bundle as a function of E_{laser} (Ref. 36). A comparison is shown in Figure 9 between experimental observations
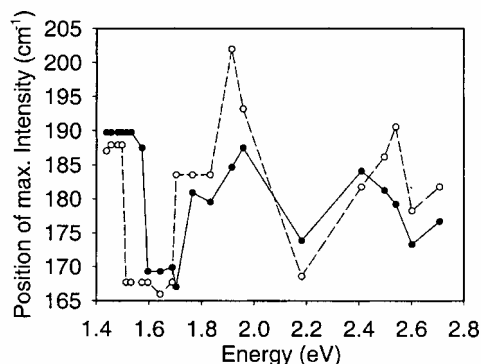
of SWNT bundles with many laser lines and calculations based on 80 SWNTs in a bundle with an average tube diameter of 1.38 nm. In analysis of the experimental data for the SWNT bundles, it is common to use a sum of Lorentzian lines to approximate the many SWNTs contributing to each observed feature. Such an approximation cannot give direct information on the number of tubes contributing to the Raman signal on the diameter distribution of the SWNT bundle sample, since different SWNTs are excited at different relative intensities for each E_{laser} value. The Kuzmany group has shown how to analyze such data properly to yield the diameter distribution in SWNT bundle samples.[36, 41] In this analysis, a model for the resonance Raman effect is used that considers an E_{ii} dependence on (n, m), following the concepts illustrated in Figure 3a, and a small natural linewidth ($\sim 3 \, \text{cm}^{-1}$), is used, as is observed for the radial breathing-mode features.[42] Thus, Figure 9 shows direct evidence from SWNT bundles for the importance of van Hove singularities in the Raman spectra for the radial breathing mode. For example, the oscillation peaking near 2.0 eV in Figure 9 is associated with the E_{11}^{M} singularities for metallic nanotubes, whereas the band from 2.2–2.6 eV pertains to the E_{33}^{S} and E_{44}^{S} singularities for semiconducting SWNTs. From Figure 9 we can see that for this SWNT bundle the metallic window for the E_{11}^{M} transition (referring to the range in E_{11}^{M} in Fig. 3a that is in resonance with all of the nanotubes in the SWNT bundle) extends from 1.7 to 2.2 eV (Ref. 36), in agreement with prior determinations of the metallic window.[43] It should be noted that for a fixed nanotube diameter, the width of E_{11}^{M} in Fig. 3a is ~ 150 meV for SWNTs with a diameter of 1.4 nm. Observations of the RBM spectra at the single-nanotube level can be employed directly to explain in detail the observations made on SWNT bundles with the use of many laser lines, as in Figure 9.

6.2. *G*-band Features

The *G* band for isolated carbon nanotubes is dominated by two high-intensity peaks (see Figs. 10a and 10b) denoted by G^+ (upper frequency ω_G^+ feature associated with carbon atom displacements along the nanotube axis) and G^- (lower frequency ω_G^- feature associated with atomic displacements in the circumferential direction).[44, 45] The upper frequency peak ω_G^+ is always close to $1591 \, \text{cm}^{-1}$, showing no significant dependence on diameter, with some small spread of the data points that may be due to chirality-dependent effects[11] associated with the trigonal warping of the constant-energy contours $E(k)$.[31, 44, 45] Experiments at the single-nanotube level show that the splitting between the frequency of the upper and lower *G*-band peaks provides a determination of d_t through the relation

$$\omega_G^- = \omega_G^+ - \mathscr{C}/d_t^2 \qquad (4)$$

Fig. 9. Frequency of the maximum intensity of the radial breathing mode for excitation with various lasers of different E_{laser} values, as measured (●) and as calculated (○) (including an 8.5% upshift in frequency associated with intertube coupling).[36] Reprinted with permission from Ref. 36, M. Milnera et al., *Phys. Rev. Lett.* 84, 1324 (2000). © 2000, American Physical Society.

where $\mathscr{C} = 47.7$ cm^{-1} nm^2 for semiconducting tubes and 79.5 cm^{-1} nm^2 for metallic nanotubes.[38] Whereas the determination of the form of Eq. (4) that expresses the diameter dependence of the G-band frequency $\omega_G^-(d_t)$ and the evaluation of the coefficient $\mathscr{C}$ are greatly aided by measurements on individual nanotubes, the results, thus obtained, can be used to account for G-band observations on SWNT bundle samples. The spread in the experimental data for both ω_G^+ and ω_G^- at constant d_t relative to Eq. (4) in Figure 10c is likely due to the spread in the E_{ii} bands at constant diameter, as shown in Figure 3a, and is related in a fundamental way to the nanotube chirality (see Fig. 8). Other factors contributing to the spread in Figure 10c may include contributions from G-band features associated with E_1 and E_2 symmetries, and how well the resonance condition is satisfied. It is important to mention that the G^- feature for semiconducting tubes and the G^+ feature for both semiconducting and metallic tubes are well described by a Lorentzian lineshape, whereas the G^- feature for metallic tubes is much broader because of the coupling between the conduction electrons and the phonons, induced by the curvature of the nanotubes. This coupling is observed to be much stronger for the case of SWNT bundles than for isolated SWNTs. For both isolated SWNTs and SWNT bundles, the broad Breit–Wigner–Fano lineshape for the G^- feature helps to provide an easy method for distinguishing semiconducting (Fig. 10a) from metallic (Fig. 10b) nanotubes.

The strong polarization effects observed experimentally for both the RBM and G-band features of the resonance Raman spectra emphasize the importance of monitoring the polarization alignment with respect to the nanotube axis when doing (n, m) characterization on individual carbon nanotubes.[46] Also, checking the linewidths of Raman spectra is often helpful for testing whether the experimental Raman system is working well. It should also be mentioned that the linewidths for the G^+ feature are significantly smaller at the single-nanotube level, going down to 6 cm^{-1}, as compared with ≥ 15 cm^{-1} for SWNT bundles. And since the electron-plasmon coupling that gives rise to the BWF lineshape is weaker in isolated SWNTs than in SWNT bundles, smaller linewidths are observed for the G^- feature for isolated SWNTs than for SWNT bundles.[42]

Finally, for special (n, m) values, when using a specific E_{laser} excitation energy, it is possible for the incident photon to be in resonance with one E_{ii} value (for example, E_{44}^S) and for the scattered photon to be in resonance with another $E_{i'i'}$ value (for example, E_{33}^S). Under these circumstances, unusual G-band profiles are observed. Such a situation is extremely sensitive (at the meV level) to the (n, m) identification and provides a sensitive corroboration for a given (n, m) assignment.[38]

6.3. D-band and G'-band Features

Other Raman features observed in SWNT bundles that are clarified by observations at the single-nanotube level are
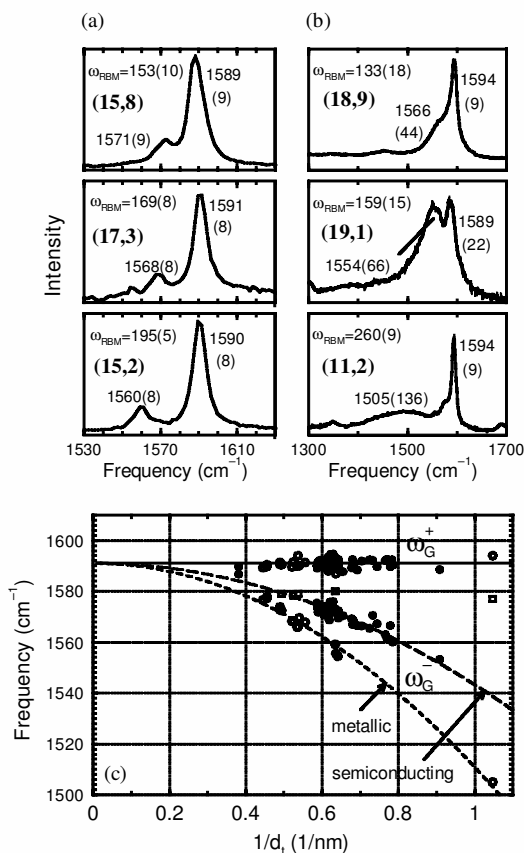

Fig. 10. (a and b) Profiles of the G-band spectra at the single-nanotube level for three semiconducting (a) and three metallic (b) isolated individual nanotubes whose (n, m) indices are determined by analysis of their RBM spectra. The frequencies for ω_G^+ and ω_G^- are indicated in cm^{-1} for each nanotube, along with the corresponding linewidths in parentheses. (c) Dependence on the reciprocal nanotube diameter $1/d_t$ of ω_G^+ and ω_G^- for both semiconducting nanotubes (solid circles) and metallic nanotubes (open circles). The open squares indicate that a peak near ~ 1580 cm^{-1} is sometimes observed in the Raman spectra for metallic SWNTs.[38] Reprinted with permission from Ref. 38, A. Jorio et al., *Phys. Rev. B* 65, 155412 (2002). © 2002, American Physical Society.

the two highly dispersive bands (see Fig. 1a) referred to as the disorder-induced D-band ($1250 < \omega_D < 1450$ cm^{-1}) and its second-order G'-band ($2500 < \omega_{G'} < 2900$ cm^{-1}, where $\omega_{G'} \simeq 2\omega_D$), which is observed whether or not disorder is present. In first-order Raman scattering experiments, in general, the phonon frequency does not depend on the laser excitation energy (as, for example, for the RBM band and the G-band in carbon nanotubes). In contrast, the D-band and G'-band are special because the frequencies of these modes depend strongly on the laser excitation energy, indicating that these bands are highly dispersive. The origin of this strongly dispersive behavior[3, 17, 47] in both graphite and SWNTs has been explained by a double resonance Raman mechanism[21, 22] involving a second-order scattering process. The Raman intensity enhancement responsible for the strong intensity of the D-band and G'-band modes in graphite and in carbon nanotubes is a resonance with both an intermediate

REVIEW

state and either the initial or final states, thus yielding a double resonance process, with strong electron-phonon coupling. This strong dispersion has been exploited in the case of carbon nanotubes, allowing us to use phonon frequency measurements, which can be made with high precision, to provide detailed information about the electronic structure, which is not easy to obtain by other experimental techniques.

In the case of nanotubes, the quantized wave vectors k_{ii}, where the E_{ii} singularities in the joint electronic density of states occur, play a fundamental role in determining the resonance process, as is clearly seen by comparing the chiral angle dependence of the phonon frequency ω_D, shown in the upper left panel of Figure 11a, with the corresponding k_{ii} vector dependence on chiral angle, shown in the lower panel of Figure 11a. As a result of this chirality dependence, it is possible to observe a D-band and a G'-band signal from different (n, m) SWNTs, using the same laser excitation energy E_{laser} but with different $E_{laser} - E_{ii}$ energy separations, indicating that the spectral features will be observed under different preresonance conditions. In the lower panel of Figure 11a, the circles denote the predicted (n, m) indices that can be resonant, and the stars within the circles denote the SWNTs that were actually observed in the single-nanotube Raman spectroscopy experiments carried out to date.[30, 37] The good agreement between the upper and lower panels in Figure 11a shows that the θ dependence of ω_D in SWNTs can be explained in terms of the relation between the wavevector $|k_{ii}|$ for electrons and the wavevector q for the phonons to which electrons are strongly coupled by the double resonance process.[21, 22] We use the relation $|q| \sim 2|k_{ii}|$ between the k_{ii} vectors for the electrons and the q vectors for the phonons (which comes from the double resonance process[22]) to provide information about the dependence of the D-band and G'-band frequencies on nanotube diameter and chirality, or equivalently on the (n, m) indices of a particular nanotube. We can use this information for many purposes, such as, for example, to predict the basic D-band and G'-band lineshapes for individual (n, m) tubes and then to compare these predictions with experimental observations, as illustrated below.

For most of the *semiconducting* tubes, the G'-band shows a single Lorentzian peak, as illustrated in the lower left panel of Figure 11b for the $(17, 7)$ SWNT. However, there are some special SWNTs that show a two-peak lineshape, as illustrated in the upper left panel of Figure 11b for the $(15, 7)$ SWNT. These different G'-band profiles can be understood by analyzing the resonant process of E_{laser} with the singularities in the JDOS shown in the right panels of Figure 11b, keeping in mind that the quantized states k_{ii} determine the G'-band frequencies $\omega_{G'}$. By examining the JDOS, we see that for the $(15, 7)$ SWNT, the laser excitation energy E_{laser} (incident photon) is resonant with E_{44}^S, whereas $E_{laser} - E_{G'}$ (scattered photon) is resonant with E_{33}^S, where each of the two resonances can
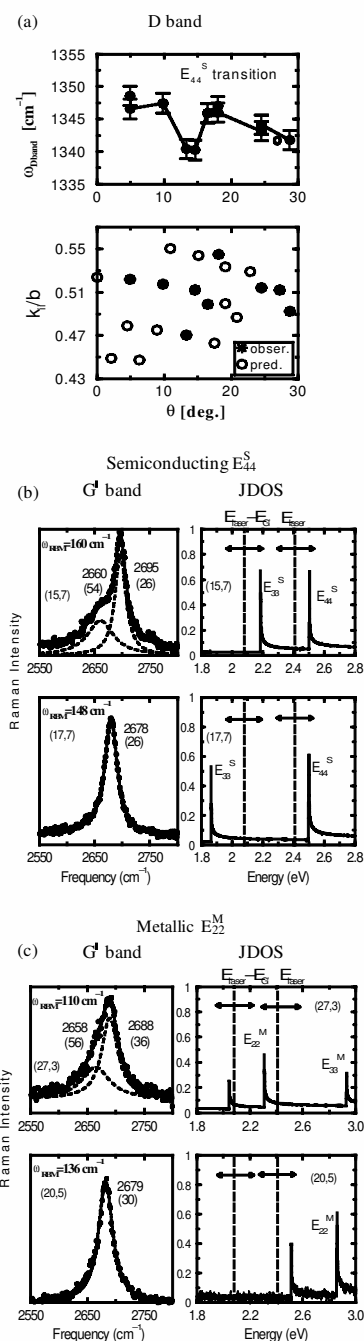

Fig. 11. (a) Measured D-band frequencies as a function of chiral angle θ of semiconducting SWNTs for which E_{laser} is in resonance with the E_{44}^S interband transitions (upper panel) and the distance $|k_{ii}|$ to the K-point for electrons in the 2D Brillouin zone of graphite (see Fig. 2b), associated with the E_{ii} van Hove singularities, plotted as open circles versus θ for the possible resonant tubes (lower panel) and as stars over the open circles for the experimentally observed tubes in the upper panel. (b) G'-band profile (left) and joint density of electronic states (right) for the $(15, 7)$ and $(17, 7)$ semiconducting SWNTs. The vertical dashed lines at 2.41 eV and 2.08 eV are for the incident and scattered photons, respectively. The horizontal double arrows denote the resonant windows for the incident and scattered photons. All frequencies (linewidths) are in units of cm^{-1}. (c) As in (b), except that the data are for the $(20,5)$ and $(27,3)$ metallic SWNTs.[37, 48] Reprinted with permission from Ref. 37, A. G. Souza et al., *Phys. Rev. B* 65, 035404 (2002). © 2002, American Physical Society.

be considered as an independent scattering process. Then, the two peaks observed for the G'-band for a $(15, 7)$ SWNT arise from resonance processes involving both k_{44} (upper frequency component) and k_{33} (lower frequency component). The possibility of observing an effect, where the two phonons resonant with *different* E_{ii} van Hove singularities are distinct in frequency, is related to the very strong dispersion of the G'-band.

In contrast, the G'-band profile in the lower left panel of Figure 11b has a single Lorentzian peak because only the incident photon is resonant for this SWNT. In fact, it is just this profile that allows the identification of this tube as a $(17, 7)$ SWNT, since the singularity E_{33}^S is too far from the energy of the scattered photon to allow the resonance process to occur. From the measured radial breathing-mode frequency $\omega_{RBM} = 148$ cm^{-1}, there are two likely (n, m) candidates for the identification of this tube, namely, the $(17, 7)$ and $(16, 8)$ SWNTs. The $(16, 8)$ option is eliminated from the assignment because the E_{33}^S energy would give rise to a strong resonance with the scattered photon, and two peaks in the G'-band lineshape would then be expected. On the basis of this argument, we conclude that the proper (n, m) assignment for this $\omega_{RBM} = 148$ cm^{-1} SWNT is $(17, 7)$.

Two peaks in the G'-band spectrum can also be observed for *metallic* tubes (see the upper left panel of Fig. 11c), but the explanation of this effect for metallic SWNTs is based on a different physical mechanism than for semiconducting SWNTs. For some metallic SWNTs, single Lorentzian peak profiles are observed experimentally, as shown in the lower left panel of Figure 11c. The two peaks in the G'-band for metallic tubes are associated with the splitting of the electronic states ΔE_{ii}^M due to the trigonal warping effect, being zero for armchair SWNTs and a maximum for zigzag SWNTs (see Fig. 2a). We show in Figure 11c the case of the $(27, 3)$ SWNT, where each component of the E_{ii}^M pair is resonant with either the incident or the scattered photon, so that two peaks will be observed in the G'-band at the single-nanotube level for this SWNT. For semiconducting SWNTs, two resonant van Hove singularities correspond to two electron wavevectors of different magnitudes, such as k_{33} and k_{44}, which in turn form two phonon wavevectors of different magnitudes, giving rise to a two-peak Raman G'-band. In contrast, for metallic nanotubes, the two resonant van Hove singularities correspond to two electron wavevectors of the same magnitude but of opposite sign, and a two-peak structure in the Raman G'-band is also observed in this case, thus, the $(20, 5)$ SWNT is observed to have a G'-band with a Lorentzian lineshape with one peak for $E_{laser} = 2.41$ eV excitation, in agreement with its JDOS, as shown in Figure 11c (lower right), where it is seen that the only resonance is for the incident photon with the lower E_{22}^M component.

By measuring these splittings $\Delta\omega_{G'}$ in the Raman spectra for SWNTs with different chiralities, it is possible to

determine the dependence of $\Delta\omega_{G'}$ on the splitting ΔE_{ii}^M of the E_{ii}^M pair due to the trigonal warping effect, which is calculated from the (n, m) values for each nanotube. From these data, a linear relation is obtained between $\Delta\omega_{G'}$ and ΔE_{ii}^M, with a zero intercept and a slope of 108 ± 5 cm^{-1}/eV. Measurements of $\omega_{G'}$ as a function of E_{laser} on SWNT bundles yield a slope for $\partial\omega_{G'}/\partial E_{laser} = 106$ cm^{-1}/eV (Ref. 49). The connection between this result on SWNT bundles and the measurement of the slope of $\Delta\omega_{G'}$ versus ΔE_{ii}^M on isolated metallic SWNTs has recently been explained as resulting from phonon anisotropy around the K point.[50]

Not only the radial breathing mode, but also the D-band and G'-band exhibit a dependence of their resonant frequencies on nanotube diameter. But for the dispersive D-band and G'-band, this effect is complicated by the chirality dependence of ω_D and $\omega_{G'}$ as discussed above. This complication is shown in Figure 12a, where the D-band
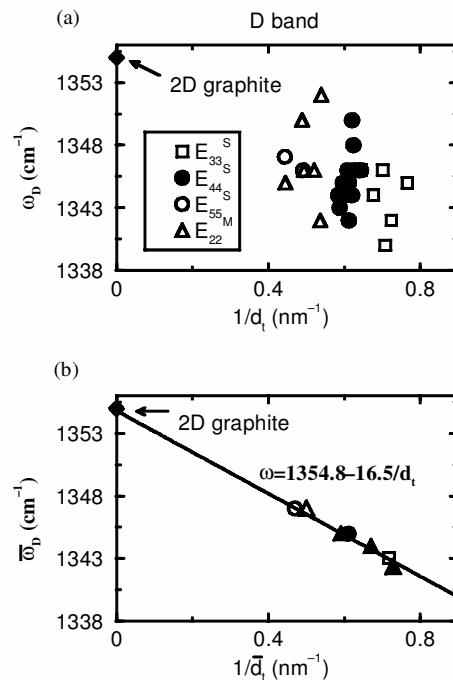

Fig. 12. (a) D-band frequencies as a function of reciprocal diameter for individual SWNTs, using $E_{laser} = 2.41$ eV laser excitation. The data are classified in terms of the E_{ii} interband transition with which the resonance occurs, including metallic and semiconducting SWNTs. (b) Plot of $[\bar{\omega}_D(E_{ii})]$, the observed D-band frequencies averaged over all tubes resonant with a given interband transition E_{ii} versus the corresponding reciprocal of the average diameter $\bar{d}_t$ of the tubes. In this plot $\bar{\omega}_D$ and $\bar{d}_t$, for the average over the isolated SWNTs, and $\bar{\omega}_D$ and $\bar{d}_t$, for the average within SWNT bundles, are both included. Data are shown for E_{laser} in resonance with the E_{55}^S, E_{44}^S, E_{33}^S, and E_{22}^M interband transitions in the JDOS. The line is a fit to the data, showing that the D-band frequencies extrapolate (on average) to the graphene (2D graphite) value when $1/\bar{d}_t \to 0$. The solid triangles in (b) stand for D-band frequencies in three different SWNT bundles with different average diameters.[49–52] Reprinted with permission from Ref. 49, M. A. Pimenta et al., *Braz. J. Phys.* 30, 423 (2000). © 2000, Brazil Physical Society.

frequency ω_D for isolated SWNTs is plotted versus $1/d_t$ for different singularities E_{ii} in the JDOS (for both semiconducting (S) and metallic (M) tubes), where the SWNT diameter was determined for each nanotube with the empirical equation $\omega_{RBM} = 248/d_t$ that is established for isolated SWNTs on a Si substrate.[4] Although these data do not show a definitive pattern for the d_t dependence of ω_D, we can see that ω_D for isolated SWNTs, in the D-band spectra taken with $E_{laser} = 2.41$ eV laser excitation, have values lower than ω_D for 2D graphite (1355 cm^{-1} taken from Ref. 53, as shown by the solid diamond in Fig. 12). We can further see that the data points seem to extrapolate roughly to the 2D graphite value when $d_t \to \infty$, that is, $(1/d_t) \to 0$. However, when these data points are appropriately averaged, the measurements at the single-nanotube level become very useful for understanding the corresponding dependence of ω_D on tube diameter in SWNT bundles. The spread in the data points in Figure 12a is associated with the chirality dependence[8] that spreads out the k_{ii} states as a consequence of the trigonal warping effect in the double resonance process, as shown in Figure 11a.[30]

To compare the results at the single-nanotube level with those for SWNT bundles and to gain an understanding of the mechanisms responsible for the D-band frequency, we average over the chirality-dependent ω_D data shown in Figure 12a for a given interband transition E_{ii}, over which the d_t values show only a small variation. We denote the resulting averages by $\hat{d}_t(E_{ii})$ and $\hat{\omega}_D(E_{ii})$, respectively, and we then plot these pairs of points in Figure 12b for $i = 3, 4, 5$ for semiconducting tubes and $i = 2$ for metallic SWNTs, using the same symbols as in Figure 12a. The results for the d_t dependence of the D-band frequencies then give a simple linear dependence of $\hat{\omega}_D$ on $1/\hat{d}_t$, that is, $\hat{\omega}_D = 1354.8 - 16.5/d_t$ (nm), as shown in Figure 12b. We also obtain very good agreement in Figure 12b between the $\hat{\omega}_D$ results for isolated tubes and the corresponding $\bar{\omega}_D$ results for SWNT bundles measured with the same E_{laser}, where the three solid triangles in Figure 12b denote $\bar{\omega}_D$ for three SWNT bundle samples with different $\bar{d}_t$ as given in Refs. 49–52. The results of Figure 12b show that $\hat{\omega}_D(E_{ii})$ for isolated SWNTs and $\bar{\omega}_D$ for SWNT bundles both increase when d_t increases, and the two data sets yield the same functional form. It is also significant that the diameter dependence of ω_D is the same, within experimental error, for semiconducting and metallic tubes. The results shown in Figure 12b give the big picture of ω_D as a function of d_t over a broad range of d_t, and the overall decrease in ω_D with decreasing d_t is due to the softening of the spring constants associated with nanotube curvature for the D-band vibrations.

Within one interband transition, E_{44}^S, for example, the D-band frequency has a tendency to *increase* when the diameter decreases[30] because, except for the trigonal warping effect that spreads out the electronic transitions, E_{ii} is proportional to $|k_{ii}|$, which in turn is proportional to

$1/d_t$,[2] where $|k_{ii}|$ is the magnitude of the quantized wave vectors measured from the K-point in the 2D graphite Brillouin zone. This behavior is the *opposite* of the averaged results shown in Figure 12b, where the lowest energies E_{ii} correspond to the smallest-diameter nanotubes. Since the nanotube diameter range for one E_{ii} is not so large for a given SWNT bundle sample, ω_D within a single E_{ii} branch is determined by the magnitude of the k_{ii} states,[30] which dominates over the curvature effect for a limited d_t range. When we jump from one singularity E_{ii} to another $E_{i'i'}$, the spring constants then become dominant, thus yielding the progression $\hat{\omega}_D(E_{55}^S) > \hat{\omega}_D(E_{44}^S) > \hat{\omega}_D(E_{33}^S)$.

If the same approach is applied to the G' band, which appears at about $2\omega_D$, the fit to the experimental data leads to $\hat{\omega}_{G'} = 2708.1 - 35.4/\hat{d}_t$ (nm). Both the frequency intercept at $1/\hat{d}_t \to 0$ and the slope for the G'-band data are consistent with the corresponding D-band behavior. The G'-band frequency of 2D graphite is 2710 cm^{-1} (taken from Ref. 53), which is close to 2708.1 cm^{-1}, and, furthermore, the slope of 35.4 cm^{-1} nm for the G'-band is very close to twice the D-band slope of 16.5 cm^{-1} nm.

Further experimental results support the above interpretation of the D-band dependence on the force constant and on k_{ii} states. The G'-band under compressive strain has a large variation (23 cm^{-1}/GPa) in comparison, for example, with 5.8 cm^{-1}/GPa for the G-band and 8.0 cm^{-1}/GPa for the RBM.[54] The large pressure coefficient for the G'-band can be attributed to the summation of two effects. First, the compressive strain increases the spring constants, resulting in an upshift of the G' band. Second, a compressive strain also upshifts the energy E_{ii} of the quantized states, which turns out to increase the magnitude of k_{ii}, thus also contributing to an increase in the G'-band frequency.[55] It is also interesting to observe that the slope $\partial \bar{\omega}_D / \partial (1/d_t)$ for the D-band is very close to that for the M-band feature near 1750 cm^{-1}, for which the slope is (-18.0 cm^{-1} nm for the M^+ feature and -16.7 cm^{-1} nm for the M^- feature). The M-band feature has also been attributed to a double resonance mechanism,[56] but in this case the phonons are close to the Γ-point rather than the K-point, as for the D-band phonons.

One of the unique features of the D-band and the G'-band spectra of SWNT bundles is a step or oscillatory behavior[49, 51, 57] superimposed on the linear E_{laser} dependence of both ω_D and $\omega_{G'}$ that is characteristic of graphite and sp^2 carbons. This oscillatory effect is shown for the G'-band in Figure 13a, but the corresponding effect also appears in a plot of ω_D versus E_{laser} for SWNT bundles,[49] and the oscillatory behavior is also related to the oscillations in Fig. 9 observed for the RBM. The deviation from a linear dispersive behavior is clearly seen in Figure 13b, where the points are obtained after subtraction of the linear solid-line fit to the experimental points in Figure 13a. The oscillatory behavior in Figure 13b is identified with quantum effects associated with the strong
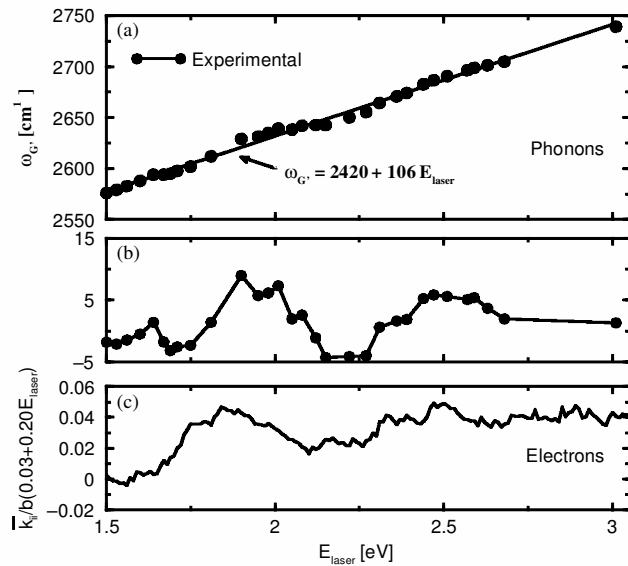
Fig. 13. (a) Dependence on the laser excitation energy of $\omega_{G'}$ for the dominant second-order Raman feature for SWNT bundles. In contrast to most sp^2 carbons, where $\omega_{G'}$ depends linearly on E_{laser}, the corresponding plot for SWNT bundles shows a superimposed step-like or oscillatory behavior near 2.0 eV and 2.5 eV for SWNT bundles.[49] (b) The oscillatory component of (a) obtained after subtracting the linear background given by $\omega_{G'} = 2420 + 106 E_{laser}$ in (a). (c) Plot of the E_{laser} dependence of the oscillations in the resonant electron wavevector k_{ii} after normalization to the length of the basis vector b of the reciprocal lattice of 2D graphite and after subtraction of the linear background. For each E_{laser} value, the k_{ii} values for each resonant SWNT are calculated, and $\bar{k}_{ii}$ represents an appropriate weighted average.[37] The strong correspondence between the E_{laser} dependence of $\omega_{G'}$ for phonons and $\bar{k}_{ii}$ for electrons provides strong support for the identification of each oscillation with a particular interband transition between van Hove singularities in the JDOS.[37] Reprinted with permission from Ref. 37, A. G. Souza et al., *Phys. Rev. B* 65, 035404 (2002). © 2002, American Physical Society.

coupling between the electrons and phonons under resonance conditions, expressed by the relation $|q| \simeq 2|k_{ii}|$ already given. Specifically the peak in $\omega_{G'}$ versus E_{laser} in Figure 13b near 2.0 eV is identified with the E_{11}^M interband transition for metallic nanotubes, and the peak near 2.5 eV is identified with the E_{33}^S and E_{44}^S transitions for semiconducting nanotubes, thus showing the importance of the 1D electronic structure of SWNTs as a basis for the physical origin of the D-band and the G'-band spectra. The plot, in Figure 13c, of the energy dependence of the wavevector at the van Hove singularities $|k_{ii}|$ normalized to the length of the basis vector b in the Brillouin zone, shows the same energy dependence for electrons as Figure 13b shows for phonons. The physical basis for this step or oscillatory behavior in Figure 13a was explained by the coupling between electrons and phonons under resonant conditions,[37] and these resonant conditions depend on both the diameter and the chirality of the nanotubes, as elucidated at the single-nanotube level in Figure 13b and c. The additional constraints imposed on energy and momentum conservation for each E_{ii} band in Figure 3a give rise to the oscillatory behavior that is superimposed

on the overall large dispersion of the G'-band frequency as the resonance wavevector moves farther and farther away from the K-point in the Brillouin zone. An independent theory by Kürti et al.[58] that considers the double resonance process in light of the van Hove singularities has also been able to explain the anomalous oscillatory dispersion that is observed in SWNT bundles.[49]

7. SUMMARY

This review of single-nanotube Raman spectroscopy emphasizes that the lineshape (frequency, intensity and linewidth) for every Raman feature depends sensitively on the nanotube (n, m) structure because the experiments are carried out under resonance conditions between the excitation photons and the singularities in the joint density of electronic states, thereby providing a close link between geometric structure, the electronic structure, and the phonon dispersion relations for carbon nanotubes at the single-nanotube level. While the radial breathing mode is the most sensitive for determining the (n, m) indices or, equivalently, the nanotube diameter and chirality, the other Raman features are independently sensitive to (n, m) and can corroborate the (n, m) identifications made with the radial breathing mode.

The Raman structural characterization experiment was shown to be easily compared with other characterization techniques for individual carbon nanotubes, insofar as it is a room-temperature measurement and is noninvasive, with a relatively weak interaction between the incident and/or scattered photons, and the electron/phonon system. Since the resonance Raman effect is only weakly interacting with carbon nanotubes, this probe results in only small perturbations to the electronic and phonon systems in comparison with other structural probes that are sensitive at the nanometer scale. Since Raman spectroscopy is a gentle probe of the electronic structure, the profile of the singularities in the joint density can be studied quantitatively. Study of the profile of the density of electronic states and of the trigonal warping of the phonon frequency contours in wavevector space remain at the cutting edge of future fundamental research in this field. On the practical side, future research is expected to focus on joint experiments using more than one experimental technique to permit other physical measurements, such as transport, mechanical properties, and thermal properties, to be done at the single-nanotube level. The availability of such experimental information can then be used further to improve the theoretical models employed in the (n, m) identification based on resonance Raman spectroscopy.

A number of unresolved issues remain for future investigation, such as the effect of the nanotube-substrate interaction on the Raman spectra, the effect of different defects, impurities, vacancies, etc. on the D-band spectra, and the dependence of the Raman intensities of the various spectral features on sample preparation conditions.

REVIEW

References and Notes

1. M. S. Dresselhaus, G. Dresselhaus, and P. C. Eklund, *Science of Fullerenes and Carbon Nanotubes,* Academic Press, New York/San Diego (**1996**).

2. R. Saito, G. Dresselhaus, and M. S. Dresselhaus, *Physical Properties of Carbon Nanotubes,* Imperial College Press, London (**1998**).

3. M. S. Dresselhaus and P. C. Eklund, *Adv. Phys.* 49, 705 (**2000**).

4. A. Jorio, R. Saito, J. H. Hafner, C. M. Lieber, M. Hunter, T. McClure, G. Dresselhaus, and M. S. Dresselhaus, *Phys. Rev. Lett.* 86, 1118 (**2001**).

5. P. A. Temple and C. E. Hathaway, *Phys. Rev. B* 7, 3685 (**1973**).

6. J. H. Hafner, C. L. Cheung, T. H. Oosterkamp, and C. M. Lieber, *J. Phys. Chem. B* 105, 743 (**2001**).

7. M. S. Dresselhaus, G. Dresselhaus, and P. Avouris, *Carbon Nanotubes: Synthesis, Structure, Properties and Applications*, Springer Series in Topics in Applied Physics, Springer-Verlag, Berlin (**2001**), Vol. 80.

8. R. Saito, G. Dresselhaus, and M. S. Dresselhaus, *Phys. Rev. B* 61, 2981 (**2000**).

9. R. Saito and H. Kataura, in *Carbon Nanotubes: Synthesis, Structure, Properties and Applications*, edited by M. S. Dresselhaus, G. Dresselhaus, and P. Avouris, Springer Series in Topics in Applied Physics, Springer-Verlag, Berlin (**2001**), Vol.80, pp. 213–246.

10. T. W. Odom, J. L. Huang, P. Kim, and C. M. Lieber, *Nature* 391, 62 (**1998**).

11. R. Saito, A. Jorio, J. H. Hafner, C. M. Lieber, M. Hunter, T. McClure, G. Dresselhaus, and M. S. Dresselhaus, *Phys. Rev. B* 64, 085312–085319 (**2001**).

12. M. S. Dresselhaus, G. Dresselhaus, K. Sugihara, I. L. Spain, and H. A. Goldberg, *Graphite Fibers and Filaments*, Springer Series in Materials Science, Springer-Verlag, Berlin (**1988**), Vol. 5.

13. H. Kataura, Y. Kumazawa, Y. Maniwa, I. Umezu, S. Suzuki, Y. Ohtsuka, and Y. Achiba, *Synth. Met.* 103, 2555 (**1999**).

14. G. Dresselhaus, M. A. Pimenta, R. Saito, J.-C. Charlier, S. D. M. Brown, P. Corio, A. Marucci, M. S. Dresselhaus, in *Science and Applications of Nanotubes,* edited by D. Tománek and R. J. Enbody, *Proceedings of the International Workshop on the Science and Applications of Nanotubes,* July 24–27, 1999, Kluwer Academic, New York (**2000**), pp. 275–295.

15. J. Kürti, H. Kuzmany, R. E. Smalley, B. Burger, M. Hulman, and A. G. Rinzler, in *Proceedings of the XII International Winter School on Electronic Properties of Novel Materials: Molecular Nanostructures*, edited by H. Kuzmany, J. Fink, M. Mehring, and S. Roth, American Institute of Physics, New York (**1998**), pp. 101–105.

16. D. Sanchez-Portal, E. Artacho, J. M. Soler, A. Rubio, and P. Ordejón, *Phys. Rev. B* 59, 12678 (**1999**).

17. M. S. Dresselhaus, G. Dresselhaus, A. Jorio, A. G. Souza Filho, and R. Saito, *Carbon* 40, 2043 (**2002**).

18. R. A. Jishi, L. Venkataraman, M. S. Dresselhaus, and G. Dresselhaus, *Chem. Phys. Lett.* 209, 77 (**1993**).

19. S. Berber, Y.-K. Kwon, and D. Tománek, *Phys. Rev. Lett.* 84, 4613 (**2000**).

20. G. S. Duesberg, I. Loa, M. Burghard, K. Syassen, and S. Roth, *Phys. Rev. Lett.* 85, 5436 (**2000**).

21. C. Thomsen and S. Reich, *Phys. Rev. Lett.* 85, 5214 (**2000**).

22. R. Saito, A. Jorio, A. G. Souza Filho, G. Dresselhaus, M. S. Dresselhaus, and M. A. Pimenta, *Phys. Rev. Lett.* 88, 027401 (**2002**).

23. A. Jorio, A. G. Souza Filho, G. Dresselhaus, M. S. Dresselhaus, R. Saito, J. H. Hafner, C. M. Lieber, F. M. Matinaga, M. S. S. Dantas, and M. A. Pimenta, *Phys. Rev. B* 63, 245416-1–245416-4 (**2001**).

24. A. G. Souza Filho, A. Jorio, J. H. Hafner, C. M. Lieber, R. Saito, M. A. Pimenta, G. Dresselhaus, and M. S. Dresselhaus, *Phys. Rev. B* 63, R241404 (**2001**).

25. Z. Yu and L. E. Brus, *J. Phys. Chem. B* 105, 6831 (**2001**).

26. T. Odom, J. H. Hafner, C. Lieber, in *Carbon Nanotubes: Synthesis, Structure, Properties and Applications*, edited by M. S. Dresselhaus, G. Dresselhaus, and P. Avouris, Springer Series in Topics in Applied Physics, Springer-Verlag, Berlin (**2001**),Vol. 80, pp. 173–212.

27. M. Canonico, G. B. Adams, C. Poweleit, J. Menendez, J. B. Page, G. Harris, H. P. van der Meulen, J. M. Calleja, and J. Rubio, *Phys. Rev. B* 65, R201402 (**2002**).

28. S. Reich, C. Thomsen, and P. Ordejón, *Phys. Rev. B* 65, 155411 (**2002**).

29. J. Maultzsch, S. Reich, and C. Thomsen, *Phys. Rev. B* 65, 1233402 (**2002**).

30. A. G. Souza Filho, A. Jorio, G. G. Samsonidze, G. Dresselhaus, M. A. Pimenta, M. S. Dresselhaus, A. K. Swan, M. S. Ünlü, B. B. Goldberg, and R. Saito, *Phys. Rev. B* 67, 085427 (1–7) (**2003**).

31. A. Jorio, M. A. Pimenta, A. G. Souza Filho, G. G. Samsonidze, A. K. Swan, M. S. Ünlü, B. B. Goldberg, R. Saito, G. Dresselhaus, and M. S. Dresselhaus, *Phys. Rev. Lett.*, 90, 107403 (**2003**).

32. H. Kataura, A. Kimura, Y. Ohtsuka, S. Suzuki, Y. Maniwa, T. Hanyu, and Y. Achiba, *Jpn. J. Appl. Phys.* 37, L616 (**1998**).

33. S. D. M. Brown, P. Corio, A. Marucci, M. S. Dresselhaus, M. A. Pimenta, and K. Kneipp, *Phys. Rev. B Rapid* 61, R5137 (**2000**).

34. P.-H. Tan, Y. Tang, C. Y. Hu, F. Li, Y. L. Wei, and H. M. Cheng, *Phys. Rev. B* 62, 5186 (**2000**).

35. Z. Yu and L. E. Brus, *J. Phys. Chem. B* 105, 1123 (**2001**).

36. M. Milnera, J. Kürti, M. Hulman, and H. Kuzmany, *Phys. Rev. Lett.* 84, 1324 (**2000**).

37. A. G. Souza Filho, A. Jorio, G. Dresselhaus, M. S. Dresselhaus, R. Saito, A. K. Swan, M. S. Ünlü, B. B. Goldberg, J. H. Hafner, C. M. Lieber, and M. A. Pimenta, *Phys. Rev. B* 65, 035404 (1–6) (**2002**).

38. A. Jorio, A. G. Souza Filho, G. Dresselhaus, M. S. Dresselhaus, A. K. Swan, M. S. Ünlü, B. Goldberg, M. A. Pimenta, J. H. Hafner, C. M. Lieber, and R. Saito, *Phys. Rev. B* 65, 155412 (**2002**).

39. A. G. Souza Filho, A. Jorio, A. K. Swan, M. S. Ünlü, B. B. Goldberg, R. Saito, J. H. Hafner, C. M. Lieber, M. A. Pimenta, G. Dresselhaus, and M. S. Dresselhaus, *Phys. Rev. B* 65, 085417 (**2002**).

40. A. Jorio, F. M. Matinaga, A. Righi, M. S. S. Dantas, M. A. Pimenta, A. G. Souza Filho, J. Mendes Filho, J. H. Hafner, C. M. Lieber, R. Saito, G. Dresselhaus, and M. S. Dresselhaus, *Braz. J. Phys.* 32, 921 **(2002)**.

41. H. Kuzmany, W. Plank, M. Hulman, C. Kramberger, A. Grüneis, T. Pichler, H. Peterlik, H. Kataura, and Y. Achiba, *Eur. Phys. J. B* 22, 307 **(2001)**.

42. A. Jorio, C. Fantini, M. S. S. Dantas, M. A. Pimenta, A. G. Souza Filho, G. G. Samsonidze, V. W. Brar, G. Dresselhaus, M. S. Dresselhaus, A. K. Swan, M. S. Ünlü, B. B. Goldberg, and R. Saito, *Phys. Rev. B* 66, 115411 **(2002)**.

43. M. A. Pimenta, A. Marucci, S. Empedocles, M. Bawendi, E. B. Hanlon, A. M. Rao, P. C. Eklund, R. E. Smalley, G. Dresselhaus, and M. S. Dresselhaus, *Phys. Rev. B* 58, R16016–R16019 **(1998)**.

44. A. Kasuya, Y. Sasaki, Y. Saito, K. Tohji, and Y. Nishina, *Phys. Rev. Lett.* 78, 4434 **(1997)**.

45. A. Kasuya, M. Sugano, Y. Sasaki, T. Maeda, Y. Saito, K. Tohji, H. Takahashi, Y. Sasaki, M. Fukushima, Y. Nishina, and C. Horie, *Phys. Rev. B* 57, 4999 **(1998)**.

46. A. Jorio, A. G. Souza Filho, V. W. Brar, A. K. Swan, M. S. Ünlü, B. B. Goldberg, A. Righi, J. H. Hafner, C. M. Lieber, R. Saito, G. Dresselhaus, and M. S. Dresselhaus, *Phys. Rev. B* 65, R121402 **(2002)**.

47. F. Tuinstra and J. L. Koenig, *J. Phys. Chem.* 53, 1126 **(1970)**.

48. A. G. Souza Filho, A. Jorio, G. G. Samsonidze, G. Dresselhaus, M. S. Dresselhaus, A. K. Swan, M. S. Ünlü, B. B. Goldberg, R. Saito, J. H. Hafner, C. M. Lieber, and M. A. Pimenta, *Chem. Phys. Lett.* 354, 62 **(2002)**.

49. M. A. Pimenta, E. B. Hanlon, A. Marucci, P. Corio, S. D. M. Brown, S. A. Empedocles, M. G. Bawendi, G. Dresselhaus, and M. S. Dresselhaus, *Braz. J. Phys.* 30, 423 **(2000)**.

50. G. G. Samsonidze, R. Saito, A. Jorio, A. G. Souza Filho, A. Grüneis, M. A. Pimenta, G. Dresselhaus, and M. S. Dresselhaus, *Phys. Rev. Lett.* 90, 027403 **(2003)**.

51. S. D. M. Brown, A. Jorio, G. Dresselhaus, and M. S. Dresselhaus, *Phys. Rev. B* 64, 073403 **(2001)**.

52. P.-H. Tan, Y. Tang, Y.-M. Deng, F. Li, Y. L. Wei, and H. M. Cheng, *Appl. Phys. Lett.* 75, 1524 **(1999)**.

53. H. Wilhelm, M. Lelausian, E. McRae, and B. Humbert, *J. Appl. Phys.* 84, 6552 **(1998)**.

54. U. D. Venkateswaran, A. M. Rao, E. Richter, M. Menon, A. Rinzler, R. E. Smalley, and P. C. Eklund, *Phys. Rev. B* 59, 10928 **(1999)**.

55. A. M. Rao, J. Chen, E. Ricther, U. Schlecht, P. C. Eklund, R. C. Haddon, U. D. Venkatesvaran, Y. K. Kwon, and D. Tománek, *Phys. Rev. Lett.* 86, 3895 **(2001)**.

56. V. W. Brar, G. G. Samsonidze, G. Dresselhaus, M. S. Dresselhaus, R. Saito, A. K. Swan, M. S. Ünlü, B. B. Goldberg, A. G. Souza Filho, and A. Jorio, *Phys. Rev. B* 66, 155418 **(2002)**.

57. A. Grüneis, M. Hulman, C. Kramberger, H. Peterlik, H. Kuzmany, H. Kataura, and Y. Achiba, in *Proceedings of the XV International Winter School on Electronic Properties of Novel Materials (IWEPNM'01)*, edited by H. Kuzmany, J. Fink, M. Mehring, and S. Roth, American Institute of Physics, Woodbury, NY **(2001)**, Vol. 591, p. 319.

58. J. Kürti, V. Zólyomi, A. Grüneis, and H. Kuzmany, *Phys. Rev. B* 65, 165433–(1–9) **(2002)**.

REVIEW